# High-Precision Stress Measurement in Thin Films for X-Ray Mirrors

by

Mallory Whalen

B.S., Massachusetts Institute of Technology (2019)

Submitted to the Department of Mechanical Engineering
in partial fulfillment of the requirements for the degree of

Master of Science in Mechanical Engineering

at the

MASSACHUSETTS INSTITUTE OF TECHNOLOGY

June 2023

Author . . . . . . . . . . . . . . . . . . . . . . . . . . . . . . . . . . . . . . . . . . . . . . . . . . . . .
Department of Mechanical Engineering
May 25, 2023

Certified by . . . . . . . . . . . . . . . . . . . . . . . . . . . . . . . . . . . . . . . . . . . . . . . . . . .
Mark L. Schattenburg
Senior Research Scientist
Kavli Institute for Astrophysics and Space Research
Thesis Supervisor

Accepted by . . . . . . . . . . . . . . . . . . . . . . . . . . . . . . . . . . . . . . . . . . . . . . . . . .
Nicolas G. Hadjiconstantinou
Professor of Mechanical Engineering
Chairman, Department Committee on Graduate Theses

# High-Precision Stress Measurement in Thin Films for X-Ray Mirrors

by

Mallory Whalen

Submitted to the Department of Mechanical Engineering
on May 25, 2023, in partial fulfillment of the
requirements for the degree of
Master of Science in Mechanical Engineering

## Abstract

Future X-ray observatories aim to achieve sub-arcsecond angular resolution with unprecedented sensitivity. Silicon meta-shell optics technology will enable the X-ray astronomy instrumentation community to create such an observatory. The lightweighted silicon mirrors used in meta-shell optics have a low stiffness which makes them susceptible to deformations caused by stress in their reflective coatings. Much research has been dedicated to figuring coated mirrors that have been deformed by their coatings and in creating low stress coatings. These coatings need to be stable over decades for the length of the observatory's mission. However, the stress stability of candidate X-ray reflective coatings has not been measured or proven to be small enough as to not re-deform the mirrors after they have been corrected.

Membrane resonance techniques have been used to study thin film stress evolution during deposition. It has a superior sensitivity as compared to other techniques, such as substrate curvature methods. A novel device that uses the membrane resonance technique to repeatably measure stress in thin films is described. Sources of non-repeatability are discussed and repeatability studies are performed. The results presented in this thesis suggest that the membrane resonance technique is suitable for use in measuring X-ray reflective coating stress stability to the minute levels required for future X-ray observatories.

Thesis Supervisor: Mark L. Schattenburg
Title: Senior Research Scientist
Kavli Institute for Astrophysics and Space Research

# Acknowledgments

My first few years in graduate school have been unconventional. A global pandemic has reshaped the way we work and interact. While not always operating under optimal conditions, I hope to have made the most of my time in graduate school so far and to have helped others at least a fraction of the amount the following people have helped me.

This work would have not been possible without my advisor, Mark, to whom I am extremely grateful. He pointed me towards the membrane resonance technique when I was sitting at my parents' dinner table wondering how I was going to continue with my studies after the Covid shutdowns were announced. Mark's encouragement to try out as many ideas as possible and fail(!) as quickly as possible along with his extreme breadth and depth of knowledge in several fields has greatly enhanced my studies.

I am indebted to Ralf, whose laser focus on the written and spoken word has pushed me to higher levels of scholarship.

My former office mates, Brandon and Heng, helped me get started in the Space Nanotechnology Lab. I would have been lost without their guidance and support. I look forward to watching their continued success in their new professorships!

Yao was always available to offer creative suggestions, even at 2 AM, when I needed them the most.

Thank you to the Izentis team for making group meeting lively and helping me when I get stuck in lab.

The members of the Women's Ice Hockey Club have let me skate out my frustrations and have become some of my closest friends.

My parents and brother have encouraged and enabled me to pursue my dreams. My wonderful partner, Alyssa, has relentlessly supported and believed in me (and has helped me get my code to run) through my time at MIT.

# Contents

# List of Figures

# List of Tables

# Chapter 1

# Introduction

Future X-ray observatories, such as the Lynx X-ray Observatory concept studied for the 2020 Astronomy and Astrophysics Decadal survey, require high resolution and high optical throughput. These requirements will be realized using silicon meta-shell optics. Meta-shell optics significantly reduce the mass and volume of the mirror assembly compared to traditional full shell optics. However, the mirrors used in the meta-shells are thin and much more susceptible to deformation from X-ray reflective coatings. This thesis discusses the development and testing of a novel tool to measure thin film stress stability. The tool can be used to quantify stress changes in candidate coatings and select the most stable thin film X-ray reflective coating for use in future X-ray telescope missions. The tool adapts a technique that relates the resonant frequency of a membrane coated with a thin film to film stress. The technique was originally used to track thin film stress during deposition runs. The tool discussed in this thesis uses the same technique, but expands it to repeatable *ex-situ* measurements.

## 1.1 X-Ray Observatories

As X-rays are strongly attenuated by most materials, including earth's atmosphere, X-ray science must be done in space with reflective optics. Additionally, X-rays are highly energetic and need to be reflected at small grazing angles. This is due to the principle of near-total external reflection where reflectivity is high for angles below the critical angle. The critical angle is proportional to $\frac{\sqrt{Z}}{E}$, the square root of atomic number, Z, of the surface material over the X-ray's photon energy, E [1,2]. High-Z materials increase the critical angle, whereas higher energy X-rays decrease the critical angle. As a result, high-Z metals such as iridium, gold, and platinum are used to reflect soft X-rays (1-10 keV) at about 1° grazing angles, and multilayer coatings are used for harder X-rays [1].

Grazing incidence reflection telescopes are typically based off of the designs of Hans Wolter [3,4]. Wolter showed that reflection off a paraboloid mirror and then a hyperboloid mirror (Wolter Type I) can focus X-rays with a wide field-of-view (FOV) without extreme coma. Figure 1-1 shows the Wolter Type I configuration with nested shells of mirrors.

The two important factors that define an X-ray telescope are angular resolution and effective collecting area. Angular resolution is the finest angular distance where two objects can be resolved from each other. It is measured using the half-power diameter (HPD) of the point spread function (PSF). HPD is the angular diameter of the image of a point source within which half of the focused X-rays are contained [1]. Effective collecting area is the geometric area of each shell that can reflect X-rays times energy-dependent terms, such as reflectivity [1]. Larger collecting area increases sensitivity.

### 1.1.1 Enhancing X-Ray Observatory Resolution

The Chandra X-ray Observatory, launched in 1999 by NASA, is currently the highest-resolution X-ray telescope with a 0.5 arc-second HPD and 0.08 $m^2$ effective area at 1 keV. It has four full shell mirror pairs that are made of 25 mm thick Zerodur and coated with iridium [5]. Next generation telescopes want to maintain or exceed this resolution while dramatically increasing sensitivity by increasing collecting area [6]. As total telescope mass is limited by rocket capabilities, the X-ray telescope community has moved away from full shell optics and has shifted to lightweight and segmented optics to achieve larger collecting areas. Table 1.1 shows the progress

| Mission | Launch Year | Mirror Technology | Angular resolution HPD (arc-second) | Mass per unit collecting area @ 1 keV (kg/m$^2$) | Production cost per unit collecting area @ 1 keV (2023 \$M/m$^2$) |
|---|---|---|---|---|---|
| Chandra | 1999 | Ground and polished shells | 0.5 | 18,000 | ~12,700 |
| XMM-Newton | 1999 | Electroformed nickel shells | 15 | 3,200 | ~465 |
| Suzaku | 2005 | Epoxy-replicated segments | 120 | 400 | ~114 |
| NuSTAR | 2012 | Slumped-glass segments | 58 | 400 | ~103 |

Table 1.1: Progress towards low mass and high collecting area X-ray telescopes. Reproduced from [7].

of creating low mass and large collecting area X-ray telescopes and the associated costs of fabrication [7]. Figure 1-2 compares the full shell optics of Chandra to the segmented shells used in NuSTAR. The Lynx X-ray Observatory (proposed for the 2020 Decadal Survey) features a 2 m$^2$ collecting area, comprised of about 40,000 0.5 mm thick silicon mirrors, with a Chandra level resolution of 0.5 arc-second HPD [8].

## 1.2 Stress in Thin Film Coatings

Thin films are deposited on substrates by a variety of methods such as sputtering, thermal evaporation, chemical vapor deposition, laser ablation, atomic layer deposition (ALD), and electrodeposition. The origins of stress in thin films, called intrinsic stresses when they arise during film deposition, depend on the method of deposition and the materials involved. Stresses in thin films have been studied extensively,

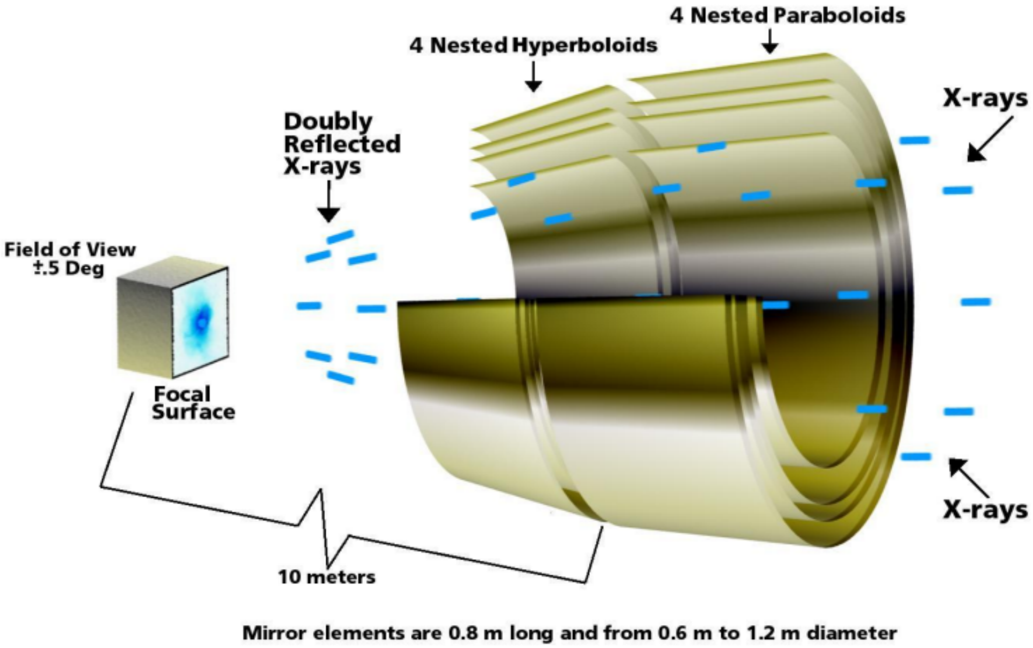

Figure 1-1: The four nested full shell pairs of the Chandra Observatory arranged in a Wolter Type I configuration. Image from [1].

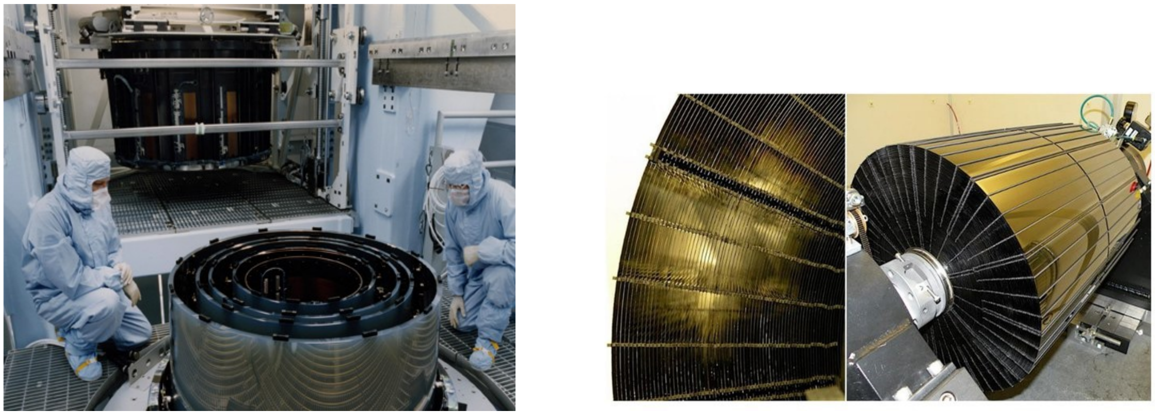

Figure 1-2: (Left) Chandra's full shell mirrors being assembled. Image from [9]. (Right) NuSTAR's segmented optics mirrors. Image from [10].

mostly driven by applications for micro-electromechanical systems (MEMS). Coatings used on X-ray mirrors are typically deposited with magnetron sputtering. Abermann shows that thin films exhibit two different types of stress vs thickness curves during deposition and classifies them as type I or type II. Type I materials, materials with a high melting point and low adatom mobility, show a monotonic increase in tensile stress with thickness. They have a columnar grain structure which results in high surface roughness. Type II materials, materials with low melting point and high adatom mobility, exhibit a compressive-tensile-compressive stress change as more atoms are deposited during deposition. Type II materials displays an island type grain structure [11]. Figure 1-3 shows the integrated stress versus film thickness curves for both types of materials. Metals deposited on silicon usually form through Volmer-Webber island growth, discussed and simulated by Seel. Initially, islands of atoms form and the stress is compressive. Then, tensile stresses arise from the coalescence of islands and increases from the creation and growth of grain boundaries. Finally, the stress relaxes due to the diffusion of adatoms into the grain boundaries [12]. After deposition, tensile stress is generated in the film due to the thermal mismatch between the cooled substrate and film [13]. Deposition parameters, such as plasma gas pressure, influence the stress profile and magnitude as well as the film density and roughness [14].

## 1.3 Effects of Thin Film Stress on Light-Weighted Optics

The typical X-ray reflective coatings, such as gold, platinum, or iridium, used on X-ray optics at a thickness of ~15 nm typically exhibit a high compressive stress of more than 1 GPa. It is well known that these coatings are capable of deforming lightweight X-ray mirrors, thus degrading the resolution of the telescope [16–18]. Finite element analysis done by Chalifoux has shown that a 0.1 N/m compressive integrated stress (approximately 7 MPa × 15 nm) change in an iridium coating on all mirrors in a

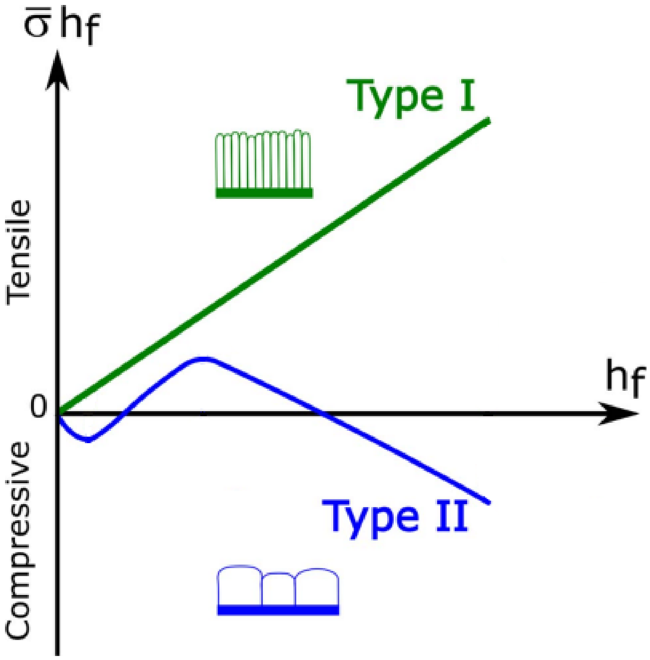

Figure 1-3: Type I and type II integrated stress versus thickness. Columnar and island type grain structure shown. Figure adapted from [15]

meta shell telescope can degrade the total resolution by 0.115 arc sec HPD [19]. The outermost mirrors of the largest radius are most affected by this stress change. A top-level angular resolution error budget given by Zhang in 2019 states that the coating must not degrade the mirror pair PSF by more than 0.1 arc sec [8].

## 1.4 Current Thin Film Stress Research

### 1.4.1 Uniform Stress Manipulation

The research addressing the deformations caused by film stress in X-ray reflective coatings is focused on either uniformly manipulating the coating to globally reduce integrated stress or non-uniformly adjusting the integrated stress to control the mirror's profile. The uniform manipulation techniques focus on lowering the film stress in single or multilayer coatings by adjusting the deposition conditions informed by monitoring integrated stress *in-situ* [20–22]. However, these techniques affect surface roughness, and the reflectivity of these coatings has not been shown to be good enough for X-ray missions. Coating both sides of the mirror to balance the integrated stress can help reduce distortions but does not totally eliminate mirror resolution degradation [18,23,24]. Annealing the film can reduce, but not eliminate, integrated stress, but it can also cause distortion at higher temperatures due to the thermal stress from the bi-material coefficient of thermal expansion (CTE) mismatch [18].

### 1.4.2 Non-Uniform Stress Manipulation

The methods that non-uniformly adjust integrated stress include ion implantation, laser micromachining, piezoelectric correction, and backside thermal oxide patterning [25–28]. These techniques measure the deformed mirror and create stress in either the mirror or a backside coating to correct the deformation. Photolithographic thermal oxide patterning has been applied to segmented Wolter-I mirrors sputter coated with 20 nm of iridium, correcting them to the 0.5 arc sec level in RMS slope errors (about 20 nm in RMS height) [29]. Most recently, Solly applied ion beam figuring (IBF) to a backside thermal oxide coating in Wolter mirrors, sputter coated with 5 nm of chromium (as a binding layer) and 30 nm of iridium), to correct them to about 7 nm RMS height. The reflectivity of these coatings was measured and shown to be suitable for X-ray missions.

Interestingly, Solly also used ALD to coat both sides of Wolter mirrors with 20 nm of platinum or a combination of platinum and aluminum oxide and produced mirrors with around 4 nm of RMS height. Reflectivity measurements were not provided [30]. ALD coatings are lower in stress but have been shown to have surface roughness at the nanometer level for electronic applications, while X-ray optics need surface roughness on the order of 5-6 angstroms [31–33].

### 1.4.3 Limitations of Current Research

While combining uniform and non-uniform stress manipulation methods corrects the immediate mirror distortions caused by coating with a reflective film, they do not address coating integrated stress stability. Yao shows stress measurements of an annealed and non-annealed chromium coatings on silicon wafers over a period of 20 days, but the stability of the annealed samples is within the repeatability of the mount [28]. The measurements were taken on a specialized low distortion wafer mount with a repeatability of ± 1 N/m [34,35]. This result does not prove annealed coatings are stable enough given Chalifoux's finding that a 0.1 N/m compressive integrated stress on all of a telescope's mirrors is enough to cause the resolution to fall out of specification. The result also shows the need for a specialized tool capable of measuring 0.1 N/m stress changes in thin films.

## 1.5 Causes of integrated stress change

### 1.5.1 Terminology

Thin film stress, $\sigma_f$ (N/m$^2$), typically has two characteristics. The first is that the film thickness, $h_f$ (m), is much thinner than the substrate thickness, $h_s$ (m). Second is that the stress state in the film is equibiaxial. X-ray mirror coatings are around 15 − 30 nm while the silicon mirrors are about 0.5 mm thick. Intrinsic film stress from amorphous or polycrystalline films is usually equibiaxial. The equibiaxial stress tensor is:

$$\sigma_f = \begin{bmatrix} \sigma_{11}^f & 0 \\ 0 & \sigma_{22}^f \end{bmatrix} \tag{1.1}$$

where $\sigma_f = \sigma_{11}^f = \sigma_{22}^f$. This stress state is also called plane stress. Plane stress occurs when the forces are applied at the boundary of the film, out of plane forces are zero, and the stress state is uniform over the thickness (it is a function of x and y only) [36]. Stress in thin films is usually of interest due to the substrate deformations that the thin films can cause. In 1909, Stoney related the stress in thin films to equibiaxial substrate curvature, $\Delta\kappa$ [37,38]. The Stoney equation for plates is:

$$\sigma_f h_f = \frac{E h_s^2}{6\left(1-\nu_s\right)} \Delta\kappa \tag{1.2}$$

The quantity $\sigma_f h_f$, the film stress times the film thickness in units of N/m, is what is responsible for the substrate curvature. Young's Modulus, $E$, is in units of Pa. The change in curvature, $\Delta\kappa$, is in of units 1/m. Poisson's ratio is $\nu_s$. To avoid ambiguity in cases where the film thickness is nonuniform or the film stress varies as an unknown function of z, integrated stress, $N_f$ (N/m), is used to describe the stress in the film.

$$N_f = \int_z \sigma_f \, dz \approx \sigma_f h_f \tag{1.3}$$

This thesis will focus on integrated stress in the film, as it is the quantity associated with deformation of substrates.

### 1.5.2 Stress Relaxation in Thin Films

Deposited films are often in a metastable state. Their grain size, defect structure, and crystal structure can all change to reduce energy [39,13]. As the films used in X-ray coatings are at least ten thousand times smaller than the silicon mirrors they are coated on, plastic deformation of the thin film accounts for all the stress relaxation.

If the thin film is thick enough, misfit dislocations of the thin film to accommodate for lattice mismatches between the film and substrate will reduce stress. However, in very thin films with small grain sizes, the energy to create a dislocation is too great for the film [39,40]. At high temperatures, such as during annealing, diffusional creep and, to a lesser extent, grain boundary sliding can relieve stresses in these small grain films. In diffusional creep of compressive films, atoms from the interior of a film migrate to the surface [40]. These relaxation mechanisms can give rise to hillocks, protrusions on the surface of a film with height typically greater than the film thickness [41]. A surface passivation layer, such as an oxide, reduces surface diffusion and can reduce hillock formation [42,43].

High temperature thermal annealing helps create a more stable grain structure through grain growth and crystallization [39]. Although annealing has been used to "stabilize" films for X-ray mirrors, there is no study showing that film relaxation remains under 0.1 N/m after annealing. A study that cyclically thermally annealed and then aged gold films measured stress relaxation after 100 days of aging [44]. Furthermore, as the coated mirrors will be kept in laboratory air for unspecified amounts of time during fabrication, the porous films can absorb water from the air. Water absorption has been shown to cause stress changes [14,45].

# Chapter 2

# Measurement of Stress in Thin Films

## 2.1 Existing Stress Measurement Methods

There are several methods to measure stress in thin films. It is important to note that not all stress measurements measure the same type of stresses. There are three types of stress that depend on the length scale of which they are measured. Macro-scale stress is stress that varies within the film over a length much larger than the size of a grain. Macro-scale stress is responsible for substrate deformation and is therefore the focus of this thesis. Meso-scale stress changes on the scale of a grain. It is caused by anisotropy of the grains in a single-phase material or by property differences in multi-phase bodies. Micro-stresses are stress changes within a grain which occur from crystalline defects such as dislocations [46,47]. Several methods exist to measure the various stress states in thin films. These include substrate curvature measurement, material removal, electron and X-ray diffraction, Raman spectroscopy, and vibrational methods [46,48]. Substrate curvature methods are currently the most widespread and simplest techniques for measuring macro stress. Material removal is destructive and not conducive to measuring changes in stress over time. Electron diffraction measures meso- and micro-scale stresses. X-ray diffraction and Raman spectroscopy are indirect stress measurements, as they measure strain (of crystalline materials only) by using lattice deformations and lattice vibrations, respectively [46,49]. The vibrational method relates the resonant frequency of a coated membrane to the macro

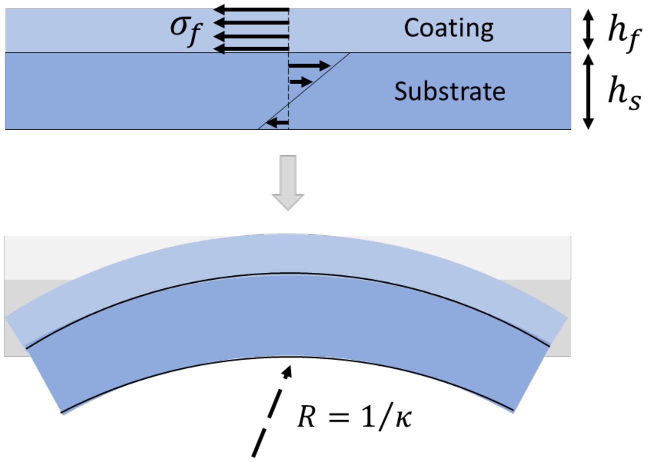

Figure 2-1: Depiction of substrate curvature showing the stress created in the substrate due to a compressive coating and resulting bending.

film stress.

### 2.1.1 Substrate Curvature Methods

Substrate curvature methods use the Stoney equation to relate substrate curvature to thin film stress. The moments created by a compressive thin film coating in a substrate and the resulting curvature are shown in Figure 2-1.

The substrate curvature method can be applied to cantilevers or plates. In the semiconductor industry, it is common to measure thin film stress of a coating by measuring wafer curvature with an optical system or a stylus profiler. Optical systems typically measure the displacement of a laser reflected from the coated substrate. Multiple beams, such as those used in the technique called multiple beam optical stress sensor (MOSS), reduce the measurement's sensitivity to substrate vibration [50,51]. MOSS is fundamentally limited by pixel accuracy in measuring beam displacements [15]. Additionally, as can be seen from the exponential in the Stoney equation, substrate thickness limits film stress sensitivity.

Substrate curvature methods can be *in-situ*, meaning that they are taken while the film is deposited, or *ex-situ*, taken outside the deposition chamber. *In-situ* methods typically have higher sensitivity as the substrate is held in place and not unrepeatably deformed by separate mountings.

Industrial examples of *ex-situ* measurement tools are the FLX and MOS UltraScan. The FLX Flexus system from Toho Technology uses laser measurements and has a repeatability of 1.3 N/m [52]. The MOS UltraScan from kSa has a 0.32 N/m repeatability, which they define as the standard deviation of stress across 10 scans. This is the same as the tool's stress resolution, 0.32 N/m [53]. It is unclear if they remount the wafer between scans; this is a factor which can dramatically reduce repeatability. A MOS tool from the same company used for *in-situ* stress measurements, measurements taken while a film is being deposited, has a 0.06 N/m resolution [54]. This value is in line with the sensitivities of research done using the approach [55].

Other examples of *in-situ* substrate curvature methods developed for researching the stress evolution in thin films include a cantilever micro-balance with sensitivity of 0.02 N/m and a temperature compensated spherometer with a 0.015 N/m sensitivity [11,56,21]. The grid reflection method with a digital image correlation algorithm may improve upon the limitations of MOSS in future [15].

*In-situ* methods of thin film stress measurement are not suitable for measuring the stress stability of potential X-ray mirror coatings. The coatings need to be kept in conditions that will match the storage conditions of the thousands of coated X-ray mirrors while they are being assembled. Additionally, measurements need to be done over the course of weeks to years on several types of coatings to determine the most optimal one. Dedicating individual vacuum chambers to each coating sample is neither cost effective or feasible.

*Ex-situ* curvature measurements suffer from mounting non-repeatability that causes deformations. The Space Nanotechnology Laboratory developed a specialized mount for thin optics that minimizes optic deformation by reducing the effects of external loads such as gravity sag, frictional forces, and thermal stress. Curvature measurements are taken using a Shack-Hartmann wavefront sensor. It was found to have a stress measurement repeatability of ± 1 N/m when the wafer is remounted after each measurement [57,35]. For the target maximum film stress change of 0.1 N/m to be measured, the repeatability of the measurement system should be about 10%

of the target value, i.e. 0.01 N/m repeatability. As *in-situ* curvature measurement techniques do not even reach this level of sensitivity, this thesis will focus on other film stress measurement techniques.

## 2.2 Membrane Resonance Technique

In addition to the substrate curvature measurement, the resonance of coated membranes can be used to determine thin film stress. The membrane resonance method was explored in the early 1990s when X-ray lithography masks, made of thin silicon membranes, were being developed and was also used for in-situ thin film stress measurement around this time [48,58–63]. The stress sensitivity of the technique is said to be 0.001 N/m [63]. Oscillating thin structures are now ubiquitous in the semiconductor industry for use in micro-electromechanical systems (MEMS), but the membrane resonance technique did not seem to evolve past the 1990s. This thesis will focus on developing an ex-situ membrane resonance tool given the superior stress sensitivity of membrane resonance over substrate curvature methods.

### 2.2.1 Membrane Resonance to Thin Film Stress

Membranes are analogous to two-dimensional elastic strings. As in strings, the resonant frequency depends on the in-plane tension and the density. For circular membranes, the wave equation takes the form of a Bessel function. Lord Rayleigh idealized the membrane as perfectly flexible, infinitely thin, and stretched in all directions by a tension that is negligibly changed during vibration. Rayleigh extensively provides the derivation for the eigenfrequencies of a circular membrane, which will not be repeated here due to length [64]. Adapting Rayleigh's derivation to include a membrane with a thin coating provides the resonant frequency of a coated circular membrane [59,65]:

$$f = \frac{1}{2.61a}\sqrt{\frac{N_m + N_f}{\rho_m h_m + \rho_f h_f}} \tag{2.1}$$

where $f$ is the resonant frequency (first mode) in Hz, $a$ is the membrane radius in m, $N$ is the integrated stress in N/m, $\rho$ is the density in kg/m$^3$, and $h$ is the thickness in m. The subscripts $m$ and $f$ refer to the membrane and the film, respectively. This equation applies to uncoated membranes as well. The terms with subscript $f$ drop out. The $N_m$ term is the residual stress in the membrane. Residual stress is created during membrane fabrication. For example, boron doping in silicon membranes shrinks the lattice and causes a residual tensile stress in the membrane [61].

The fact that the resonant frequency of a membrane is not influenced by Young's modulus is of note. Substrate curvature methods using the Stoney equation rely on Young's modulus. As Young's modulus changes with temperature and may be imprecisely measured, it can introduce error in the substrate curvature stress measurement.

# Chapter 3

# Membrane Deflection Modelling

## 3.1 Thin Plate Theory

The required force needed to vibrate a membrane can be analytically determined by leveraging membrane deflection modelling.

Thin plate theory can be used to model the deflection of a membrane. When a plate deforms, it experiences stress from bending moments as well as in-plane tensile stress from stretching of the midplane, known as membrane stress. For deflections less than the thickness of the plate, bending stress dominates and midplane stretching is negligible. For deflections greater than 1.5 the height of the plate, midplane stretching dominates and bending stress is negligible. Deflections in this regime are called membrane deflections. The change mathematically corresponds to when the vertical plate center deflection transitions from being proportional to the transverse loading pressure to being proportional to the cube root of transverse loading pressure. When deflections are on the order of plate thickness, an intermediate regime exists where both stress from bending moments and midplane stretching must be considered [66].

Kirchhoff-Love plate theory, for use where plate deflection is smaller than plate thickness, was extended for use in larger plate deflection by von-Kármán to include mid-plane stretching. The von-Kármán equations are nonlinear and notoriously hard to solve. Many different approximate analytical solutions have been derived over the years. Y. Zhang has compiled many of the derived solutions to predict the deflections of clamped circular plates [67].

To accurately model all deflection regimes encountered in vibrational testing, this thesis will use a solution for the intermediate range of deflection where membrane stress is considered as well as bending stress. The Timoshenko and Woinowsky-Krieger solution will be used, with slight modifications provided by Y. Zhang to keep the Poisson's ratio a variable and to include the effects of initial midplane stretching [66,67]. Timoshenko assumed the following deformation shapes for a circular membrane, clamped at the boundary and under initial in-plane tension $N_0$ (N/m) and uniform transverse pressure $q$ (normal to surface of the membrane, N/m$^2$), shown in Figure 3-1:

$$w = w_0 \left(1 - \frac{r^2}{a^2}\right)^2 \tag{3.1}$$

$$u = r\left(a - r\right)\left(C_1 + C_2 r\right) \tag{3.2}$$

Where $w$ is the vertical displacement (m), $w_0$ is the deflection of the membrane center (m), $r$ is the radial position (m), $a$ is the membrane radius (m), $u$ is the radial displacement (m), and $C_1$ and $C_2$ constants. $w_0$, $C_1$, and $C_2$ are found by minimizing the strain energy due to bending and stretching. Y. Zhang provides the force to center displacement relationship for this deformation shape:

$$w_0 + \left[\frac{3}{4}\left(\frac{a}{h}\right)^2 \left(1+\nu\right)\epsilon_0\right] w_0 + \left(0.4319 + 0.2411\nu - 0.1808\nu^2\right)\frac{w_0^3}{h^2} = \frac{qa^4}{64D} \tag{3.3}$$

Where

$$\epsilon_0 = \frac{\left(1-\nu\right)N_0}{Eh} \tag{3.4}$$

The first term, $w_0$, is due to bending. The second term is due to the initial midplane stretching. The third term is due to further midplane stretching. $N_0$ is equivalent to $N_m$, the residual stress in the membrane when there is no thermally induced stress. Finding the real root of this equation gives $w_0$.

The flexural rigidity, $D$ (Nm), is given by:

$$D = \frac{Eh^3}{12\left(1-\nu^2\right)} \tag{3.5}$$

Y. Zhang also gives the constants and traditional equations for radial and tangential tension [67]:

The constant $C_1$:

$$C_1 = \left[\frac{35}{4}\left(0.146 - 0.2603\nu\right) + \frac{45}{4}\left(0.0127 + 0.13968\nu\right)\right]\frac{w_0^2}{a^3} \tag{3.6}$$

The constant $C_2$:

$$C_2 = \left[-\frac{45}{4}\left(0.146 - 0.2603\nu\right) - \frac{75}{4}\left(0.0127 + 0.13968\nu\right)\right]\frac{w_0^2}{a^4} \tag{3.7}$$

The radial tension, $N_r$ (N/m), is:

$$N_r = \frac{Eh}{1-\nu^2}\left[\frac{du}{dr} + \frac{1}{2}\left(\frac{dw}{dr}\right)^2 + \nu\frac{u}{r}\right] + N_0 \tag{3.8}$$

The tangential tension, $N_t$ (N/m), is:

$$N_t = \frac{Eh}{1-\nu^2}\left[\frac{u}{r} + \nu\frac{du}{dr} + \frac{\nu}{2}\left(\frac{dw}{dr}\right)^2\right] + N_0 \tag{3.9}$$

The tensions can be averaged across the whole membrane to get the mean tension:

$$N_\alpha^{mean} = \frac{1}{\pi a^2}\int_0^a N_\alpha\left(r\right) 2\pi r \, dr \tag{3.10}$$

$$N_{mean} = \begin{bmatrix} N_r^{mean} & 0 \\ 0 & N_t^{mean} \end{bmatrix} = \frac{1}{2}\left(N_r^{mean} + N_t^{mean}\right) \tag{3.11}$$

The $\alpha$ in $N_\alpha$ is a dummy variable for $r$ and $t$. Using the above equations, the average tension, or average integrated stress, in the membrane can be solved for with respect to membrane properties and loading pressure. The resonant frequency of the membrane can be calculated with this average tension.

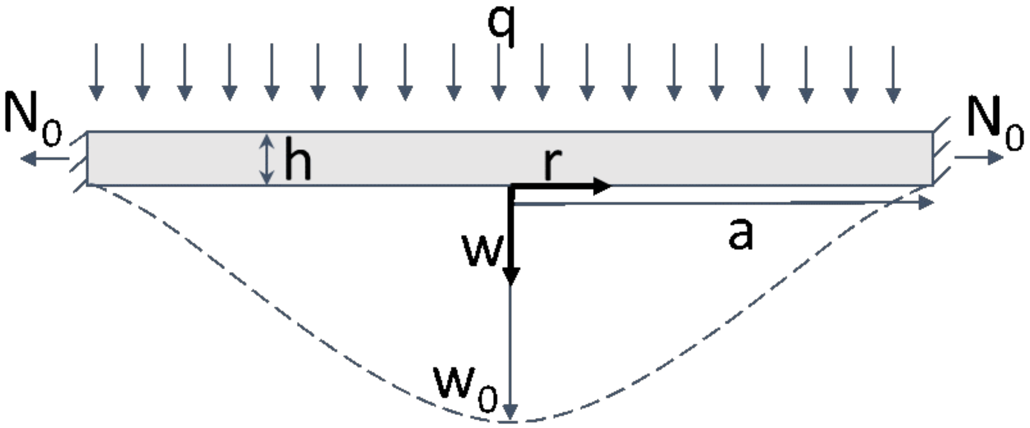

Figure 3-1: Timoshenko membrane deflection shape for clamped membrane under traverse pressure load with parameters shown.

Equation 2.1 relates the resonant frequency and tension of a membrane. It was derived without considering the bending stress. To show that Equation 2.1 is valid, the full equation for resonance of a membrane that includes the plate bending term is [68]:

$$f = \frac{\alpha_{m,n}}{2\pi a}\left(\frac{N}{\rho}\right)^{1/2}\left(1+\frac{\alpha_{m,n}^2 D}{a^2 N}\right)^{1/2} \tag{3.12}$$

$\alpha_{m,n}$ is the eigenvalue of the Bessel function of the $m^{th}$ kind and $n^{th}$ degree. This equation reduces to Equation 2.1 when the last term, the plate bending term, is much less than one. As $D$, the flexural rigidity, of a 2 $\mu$m thick silicon is about $1 \times 10^{-7}$ Nm, the radius is in the millimeter range, and residual stresses in these types of membranes can be up to 100 MPa, the plate bending can be ignored and Equation 2.1 suffices [69].

Deriving the full equations for radial and tangential tensions is intensive. Instead, symbolic computation was done with Mathematica to plot the relationships between quantities and determine relative scaling.

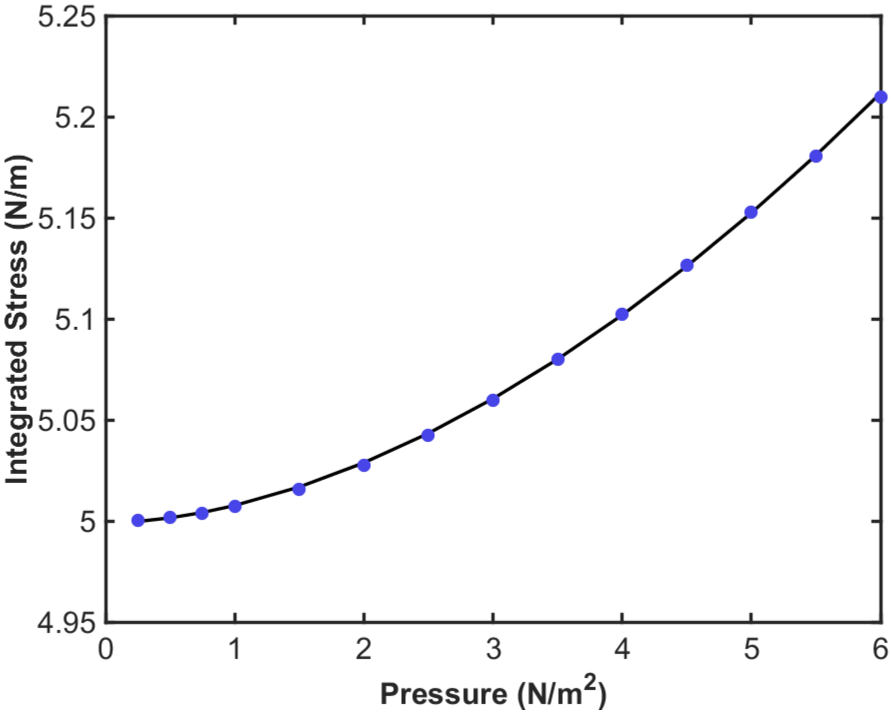

Figure 3-2: Integrated stress versus pressure for a silicon membrane with a 3 mm radius, 2 $\mu$m thickness, and 5 N/m residual stress. The fit is $0.009q^{1.79}+4.999$.

## 3.2 Device Parameter Selection

Figures 3-2 through 3-5 show the effect of transverse pressure and then membrane thickness on integrated stress and resonant frequency. Figure 3-6 shows how membrane radius relates to resonant frequency. Membrane geometry can be chosen from these relationships. For this thesis, boron doped <100> Single Crystal Silicon membranes were chosen and were fabricated by the company Norcada. Larger radii are favorable as they produce lower frequency resonances in the kilohertz range, which can be measured and recorded with standard equipment. As the radius increases, frequency sensitivity to variations in radius decreases. However, price per membrane goes up as the membrane covers more area on a silicon wafer. A membrane with a radius of 3 mm $\times 0.08\mu$m were used for this thesis. Membrane thickness determines if the membrane will behave as a membrane or a plate as well as the resonance frequency band. According to the manufacturer, too thin of a membrane will buckle

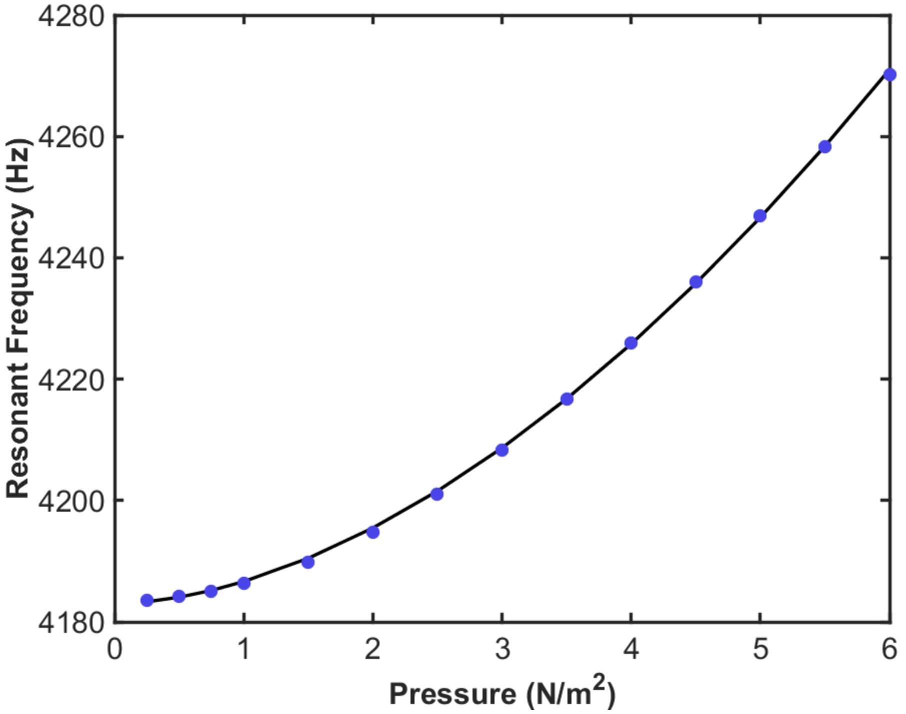

Figure 3-3: Resonant frequency vs pressure for a silicon membrane with a 3 mm radius, 2 $\mu$m thickness, and 5 N/m residual stress. The fit is $3.639q^{1.778}{+}4183$.

from too little residual stress. Norcada specified that membranes of a 3 mm radius below 2 $\mu$m in thickness will buckle. Membranes with a thickness of 2.0 ± 0.5 $\mu$m are used for this thesis. The membranes are etched into 300 ± 10 $\mu$m thick, 10.0 ± 0.2 mm square silicon frames. Increased frame length decreases how many membrane units can be produced from a single wafer, which increases price per membrane.

A circular 3 mm radius, 2 µm thick membrane with a 5 N/m residual stress etched into a 300 µm thick 10 mm square silicon frame will be referred to as the nominal device. Table 3.1 summarizes the device parameters used in this thesis.

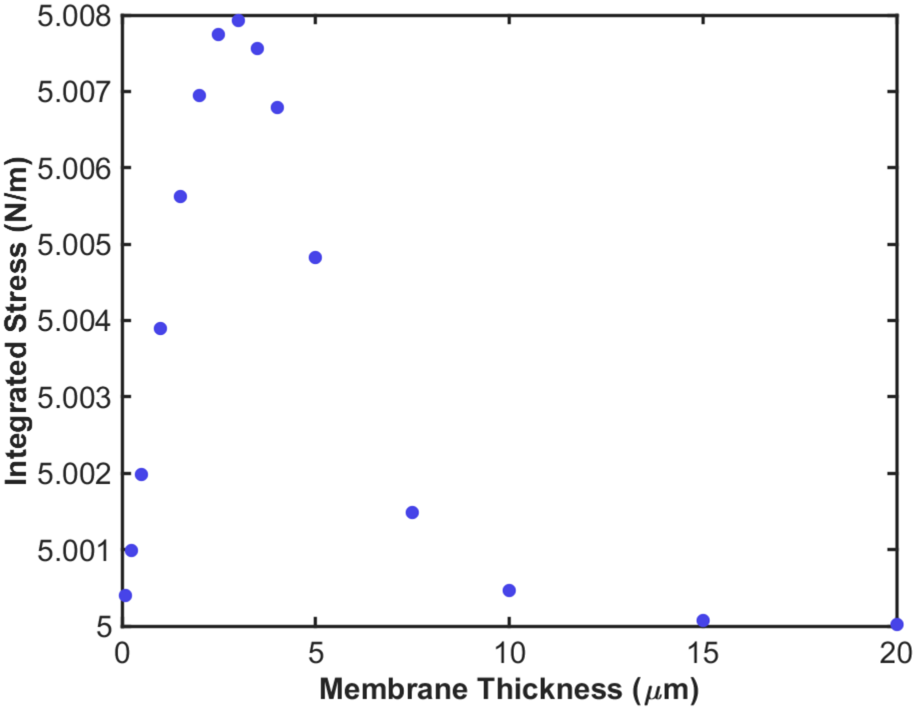

Figure 3-4: Integrated stress versus membrane thickness for a silicon membrane with a 3 mm radius and a 5 N/m residual stress under a 1 N/m$^2$ transverse pressure. The integrated stress response is interesting. Membrane thickness appears both in plate flexural rigidity and membrane stretching terms. Membrane stretching dominates until the plate becomes too thick and barely bends under the pressure.

| Parameter | Symbol | Value |
|---|---|---|
| Young's Modulus | $E$ | 169 GPa |
| Poisson's Ratio | $\nu$ | 0.22 |
| Radius | $a$ | 3 mm |
| Membrane Thickness | $h_m$ | 2 $\mu$m |
| Frame Thickness | $h_s$ | 300 $\mu$m |
| Residual Stress | $N_0$ | 5 N/m |
| CTE | $\alpha$ | $2.6 \times 10^{-6}$/°C |
| Density | $\rho$ | 2330 kg/m$^3$ |

Table 3.1: Nominal device parameters used in simulations and calculation.

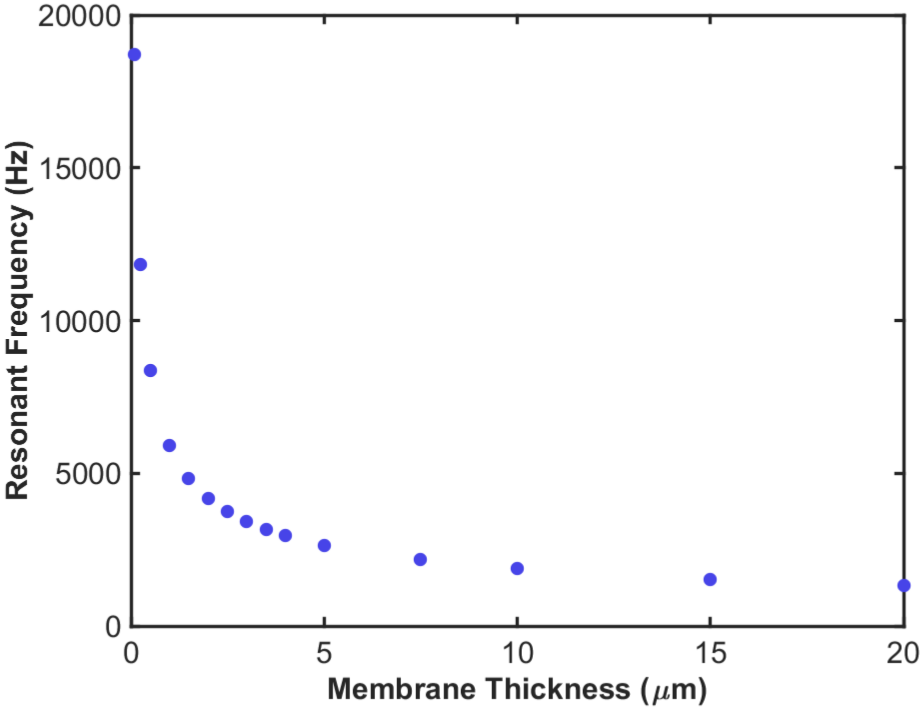

Figure 3-5: Resonant frequency vs membrane thickness for a silicon membrane with a 3 mm radius and a 5 N/m residual stress under a 1 N/$m^2$ transverse pressure. The membrane becomes less sensitive to thickness variations around 2 $\mu$m in thickness.

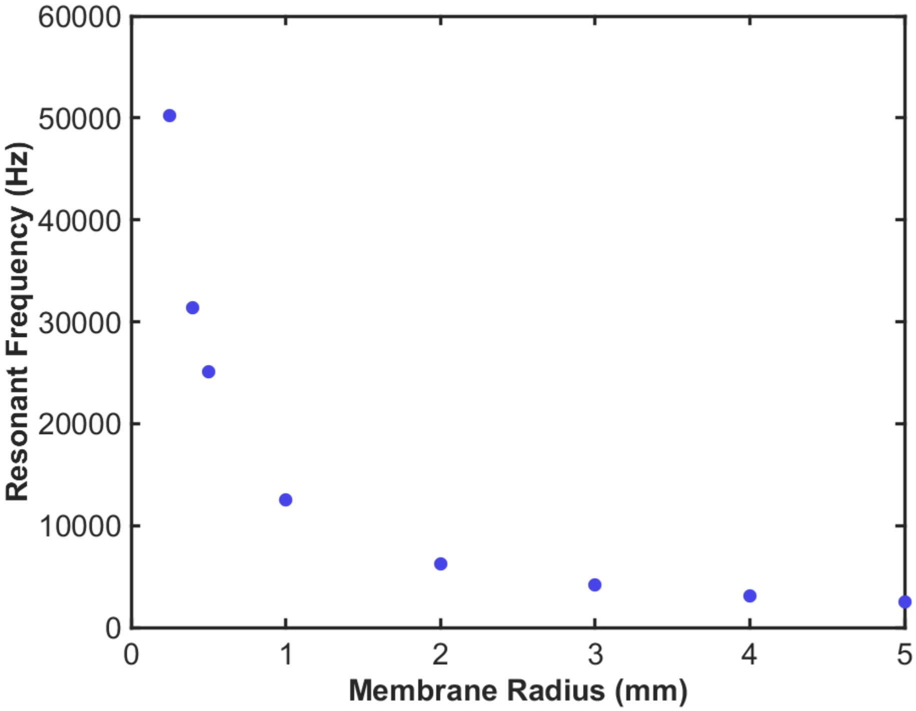

Figure 3-6: Resonant frequency vs membrane radius for a silicon membrane with a 2 $\mu$ m in thickness and a 5 N/m residual stress under a 1 N/m$^2$ transverse pressure. The resonant frequency becomes less sensitive to changes in membrane radius around 1 mm.

# Chapter 4

# Membrane Actuation

## 4.1 Types of Actuation

The membrane needs to be actuated to induce vibrations. Electrostatic force, Lorentz force, acoustic pressure, or a mechanical shaker have been used to create vibrations of membranes [62,70,59,60]. Additionally, membrane vibrations are significantly damped by air. The effects of air loading on resonant frequency are given by [58]:

$$f_{air} = f\left[1 + 1.34\frac{\rho_a a}{\rho_m h_m}\right]^{-1/2} \tag{4.1}$$

Where $f$ is the resonant frequency (Hz) in vacuum, $f_{air}$ is the resonant frequency (Hz) of a membrane at atmospheric pressure, $\rho_a$ and $\rho_m$ are the densities of air and the membrane (kg/m$^3$).

The membrane actuation technique should be able to be done in vacuum to avoid resonant frequency changes with air pressure, which can be affected by changes in temperature and humidity. Acoustic pressure induced vibrations are not suitable for use in vacuum.

Mechanical shakers or impact tests could excite resonant modes of the structure. Additionally, since the shaker would vibrate the whole apparatus, the membrane could potentially vibrate out of position.

Electrostatic force, or Lorentz force from a circular coil, are therefore the most

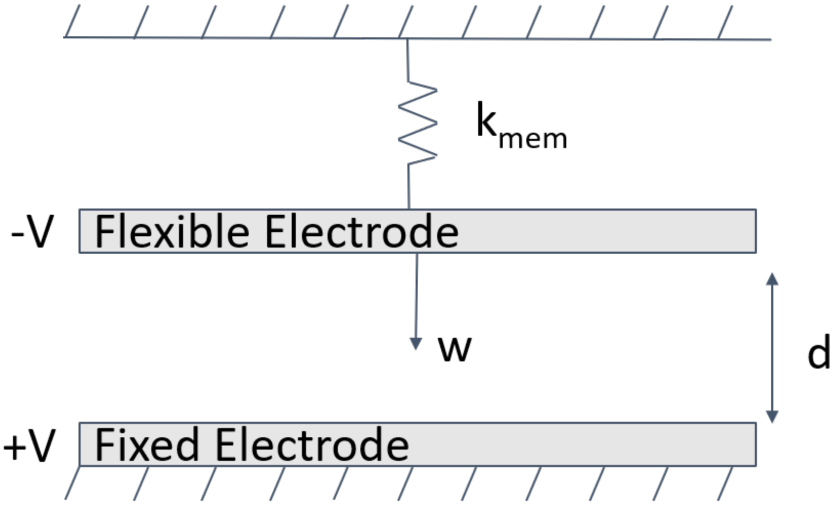

Figure 4-1: Schematic of parallel plate capacitor where the membrane stiffness is the resorting force.

applicable actuation methods as they can be used in vacuum; they will only apply force to the membrane itself and not the mechanical structure or frame the membrane is etched into. Electrostatically actuated MEMS dominate the industry and are the focus of a multitude of research efforts [71]. For example, capacitive micromachined ultrasonic transducers (CMUTs) use electrostatics to actuate a flexible circular plate to produce ultrasound [72]. This thesis uses electrostatic actuation to excite the membrane due to its simplicity and fast actuation response compared to magnetic actuation [73].

## 4.2 Electrostatic Modelling

Electrostatically actuated MEMS are modelled as variable gap capacitors. A flexible electrode is suspended above a fixed electrode. DC voltages induce displacements of the flexible electrode. AC voltages superimposed on DC voltages are used in resonators to harmonically excite the flexible electrode [71]. The membrane acts as the moveable electrode and is positioned over a fixed electrode. The membrane is heavily boron doped with 0.01 Ωcm to 0.02 Ωcm resistivity. This enables uncoated membranes to act as electrodes.

When a small displacement $\Delta w$ occurs that moves the moveable electrode toward the fixed electrode, the resulting electrostatic force, $F_{elec}$, in Newtons is [74]:

$$F_{elec} = \frac{1}{2}\frac{dC}{dw}V^2 \tag{4.2}$$

Where $C$ is the capacitance (F) and $V$ is the constant drive voltage (V).

For a parallel plate capacitor, as shown in Figure 4-1, the capacitance is:

$$C = \frac{\epsilon_0 A}{d - w} \tag{4.3}$$

Where $A$ is the area of the plate (m$^2$), $d$ is the initial distance between plates (m), and $w$ is the distance the moveable electrode displaces (m). $\epsilon_0$ is the permittivity of free space, 8.854 × $10^{-12}$ F/m.

As the membrane deflection magnitude varies radially, an average displacement, $w_{avg}$ (m) is:

$$w_{avg} = \frac{1}{\pi a^2}\int_0^a w\left(r\right) 2\pi r \, dr = \frac{w_0}{3} \tag{4.4}$$

The capacitance can be found as a function of membrane displacement and average membrane displacement [72]:

$$C = \int_0^a \frac{2\pi r \epsilon_0}{d - w_0\left(1 - \frac{r^2}{a^2}\right)^2} \, dr = \frac{\epsilon_0 \pi a^2 arctanh\left(\sqrt{\frac{w_0}{d}}\right)}{\sqrt{dw_0}} = \frac{\epsilon_0 \pi a^2 arctanh\left(\sqrt{\frac{3w_{avg}}{d}}\right)}{\sqrt{3dw_{avg}}} \tag{4.5}$$

Taking the derivative yields the electrostatic force [72]:

$$F_{elec} = \frac{1}{2}V^2\left[\frac{\epsilon_0 \pi a^2}{2dw_{avg}\left(1 - \frac{3w_{avg}}{d}\right)} - \frac{C}{2w_{avg}}\right] \tag{4.6}$$

The forces acting on the membrane are the electrostatic force, $F_{elec}$, and the mechanical restoring force, $F_m$. $F_m$ is equal to $q\pi a^2$. At equilibrium, the forces are equal and opposite, $-F_m = F_{elec}$. Rearranging Equation 3.3 to be in terms of stiffnesses and average displacement gives the form of $F_m = k_1 w_{avg} + k_2 w_{avg}^3 = q\pi a^2$. By setting $w_0$, and thus $w_{avg}$, $F_m$ can be numerically solved for using Equation 3.3. Using the equilibrium equation, the electrostatic force is equal to the mechanical restoring force, and Equation 4.6 can be rearranged to solve for the voltage required to achieve a certain membrane displacement. The force of gravity has been ignored and assumed to factor into the measured membrane residual stress term. The voltage required to achieve the set displacement can be solved for.

### 4.2.1 The Pull-In Condition

It is important to note that if the electrostatic force is greater than the restoring force of the membrane, equilibrium will not hold and the system will become unstable as the membrane collapses to the bottom electrode. The voltage where the system goes unstable is called the pull-in voltage. Figure 4-2 shows the center displacement of the membrane versus the applied voltage between the electrodes for a silicon membrane with a 3 mm radius, 2 $\mu$m thickness, and 5 N/m residual stress with an electrode separation of 100 $\mu$m. Fargas-Marques et al. discuss common pull-in conditions and derive the pull-in displacement for resonant electrostatic actuators. They state that for a static parallel plate capacitor where the mechanical restoring force is linear with displacement, i.e. a plate where the $k_2$ term is zero, the typical pull-in displacement is 1/3 of the initial plate separation distance. For the nominal device parameters, this condition would mean a pull-in voltage of around 5,000 V. In parallel plate capacitors that have a completely nonlinear restoring force, i.e. midplane stretching dominates and $k_1$ is zero, the typical pull-in displacement is 3/5 of the initial plate separation distance. At resonance, the pull-in displacement is about 1/2 of the initial plate separation [75]. As displacing the membrane a great deal creates stress that will obscure thin film stress measurements, the devices will be operated far from the pull-in conditions. Figure 12 shows that about 60 V causes center displacement of 1% for the assumed membrane properties.

The applied voltage, $V$, is the sum of the DC and AC voltages:

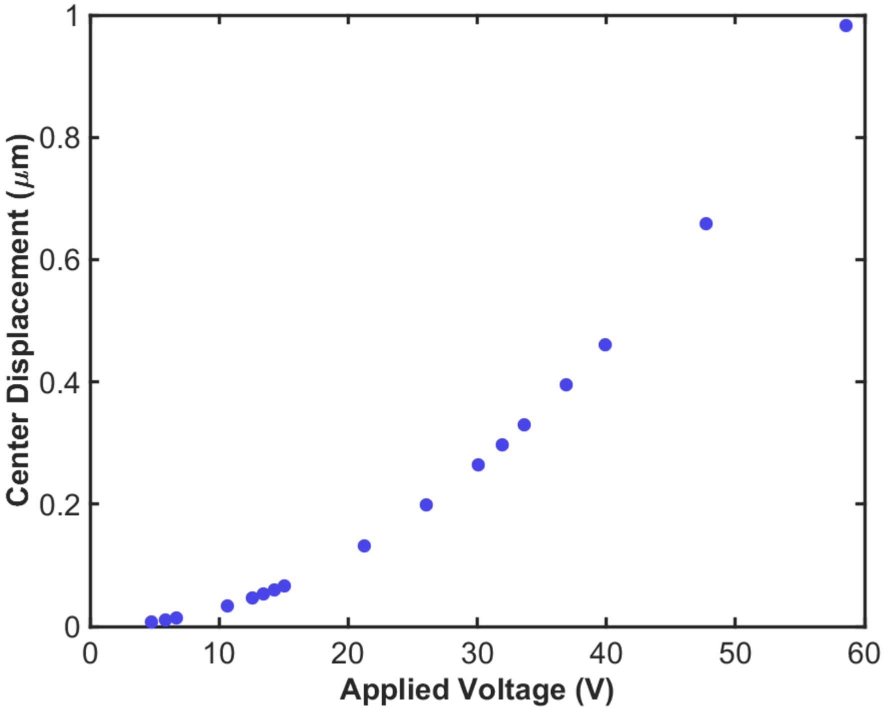

Figure 4-2: Center displacement of the membrane versus applied voltage for a silicon membrane with a 3 mm radius, 2 $\mu$m thickness, and 5 N/m residual stress with a 100 $\mu$m initial separation between the electrodes in the capacitor. Displacement goes with voltage squared.

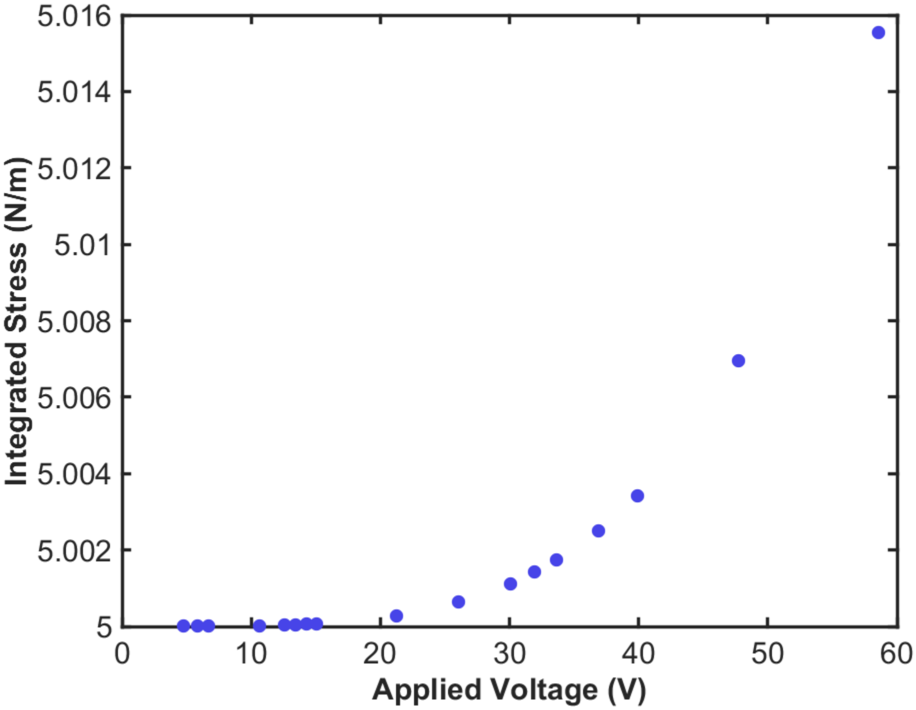

Figure 4-3: Integrated stress of the membrane versus applied voltage for a silicon membrane with a 3 mm radius, 2 $\mu$m thickness, and 5 N/m residual stress with a 100 $\mu$m initial separation between the electrodes in the capacitor. 47.6 V corresponds to $q = 1$ N/m$^2$. Integrated stress is proportional to V$^{3.76}$. These voltages are well below the pull-in voltage of about 5,000 V that results from the most conservative pull-in conditions.

$$V = V_{DC} + V_{AC} = V_{DC} + v_0 \sin(\omega t) \tag{4.7}$$

where $v_0$ is the AC amplitude in volts and $\omega$ is the frequency in rad/s. The DC voltage provides the static displacement and the AC voltage drives the membrane vibration.

### 4.2.2 Actuation Voltage to Integrated Stress

Given the voltage (and thus transverse pressure $q$), the integrated stress of the membrane can be calculated. Figure 4-3 shows the integrated stress of the membrane versus applied voltage for the chosen membrane parameters. For voltages lower than 30 V, the change in integrated stress is less than 0.001 N/m. For less than 15 V, the change in integrated stress is less than 0.0001 N/m and center displacement is on the order of 10s of nanometers. For actuation voltages lower than 30 V, the stress induced by the electrostatic force will not significantly interfere with the stress measurement and small changes in actuation voltage will not introduce non-repeatability in the stress measurement of interest. Additionally, the voltage needs to be kept low enough to ensure that the membrane does not behave nonlinearly as a Duffing spring due to large deflection [76].

# Chapter 5

# Temperature Induced Stress

## 5.1 Frame and Membrane CTE Mismatch

As materials expand upon heating according to their coefficient of thermal expansions (CTE), they develop thermal strain, which creates stress when the material is not free to expand. The residual stress in the membrane is temperature dependent as the membrane is coupled to the silicon frame it is etched into. As the membrane is doped with boron, Berry and Pritchet explain that it has a slightly different CTE than pure silicon. Berry and Pritchet describe that the often ignored effect from Young's modulus temperature dependence becomes important when the CTEs of the materials are close, such as in silicon and boron doped silicon [77]. They give the equation for temperature dependent stress in the membrane as:

$$N_m = N_0 + \beta \Delta T N_0 + \frac{E}{1-\nu} \Delta\alpha \Delta T h \tag{5.1}$$

The material properties are taken with respect to the membrane. The residual stress is $N_0$ (N/m), $\beta$ ($/^{\circ}C$) is the temperature coefficient of Young's modulus, $\Delta T$ ($^{\circ}C$) is the change in temperature, and $\Delta\alpha$ ($/^{\circ}C$) is the differential CTE defined as the CTE of the membrane subtracted from the CTE of the frame. Berry and Pritchet give $\Delta\alpha$ as -1.1 $\times$ $10^{-8}$ $/^{\circ}C$ and $\beta$ as -3.7$\times$ $10^{-5}$ ($/^{\circ}C$) for a heavily Boron doped membrane etched into pure silicon. Figure 5-1 shows the integrated stress change

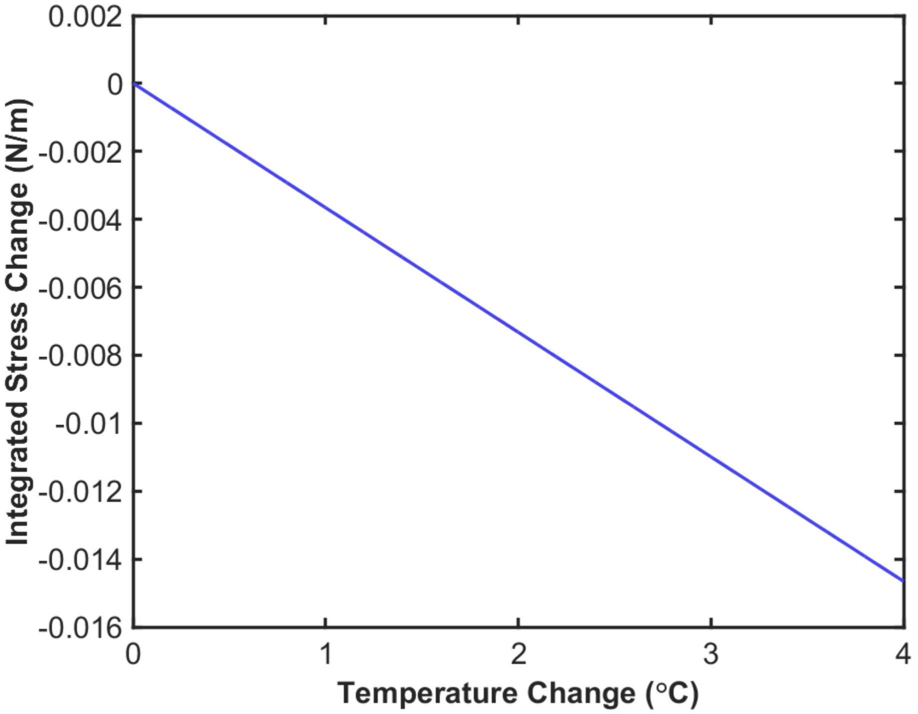

Figure 5-1: Integrated stress change in the membrane versus temperature due to differential CTEs between the frame and membrane and temperature dependence of Young's modulus. The nominal membrane properties were used. A 0.1°C change results in an integrated stress decrease of $3.5 \times 10^{-4}$ N/m.

in the membrane versus change in temperature. The membrane expands slightly more than the frame, reducing tension, causing integrated stress to decrease with temperature.

## 5.2 Coating and Membrane CTE Mismatch

In addition to thermal stresses caused by the different material properties in the device, thermal stress also arises from coating the membrane with a metal. The film is assumed to be 15 nm of iridium. As the film thickness divided by the membrane thickness is less than 0.01, a zero order approximation for the stress distribution in both the membrane and film can be used [78]:

$$\sigma_m = \frac{2\left(3z + 2t_m\right)}{h_m^2} \frac{E_f}{\left(1 - \nu_f\right)} \left(\alpha_f - \alpha_m\right) \Delta \mathrm{T} h_f \tag{5.2}$$

$$\sigma_f = \frac{E_f}{(1-\nu_f)}\left(\alpha_m - \alpha_f\right)\Delta T \tag{5.3}$$

The subscripts $f$ and $m$ refer to the film properties and the membrane properties, respectively. $z$ is the height of the membrane that spans from $z = -h_m$ to 0. Integrating these equations to get integrated stress yields:

$$N_m = -N_f = \frac{E_f}{(1-\nu_f)} h_f \left(\alpha_f - \alpha_m\right)\Delta T \tag{5.4}$$

In this zero-order approximation, the integrated stress in the membrane cancels the stress in the film. As the resonant frequency depends on $N_m + N_f$, a frequency shift will not occur due to the membrane coating. However, since the frame will also be coated, frame bending will occur to accommodate the thin film stress. The frame radius of curvature is assumed to be approximated by Stoney's equation:

$$\kappa = \frac{6h_f \frac{E_f}{(1-\nu_f)}\left(\alpha_f - \alpha_s\right)\Delta T}{\frac{E_s}{1-\nu_s} h_s^2} \tag{5.5}$$

The frame's properties are denoted by the subscript $s$. The curvature of the substrate is $\kappa$ in units of 1/m. Figure 5-2 shows frame curvature due to thermal stress in the film versus the temperature change. Frame curvature to integrated stress in the membrane will be addressed in a section 6.1.2. Positive temperature change will result in tensile stress that bends the frame to be concave up.

## 5.3 Frame to Holder CTE Mismatch

The device will also develop temperature induced stress if it is bonded to or sitting on a material with a different CTE. In the case of bonding, the induced stress can be modelled similarly to a bi-metallic strip. For a silicon device bonded to a material the strain is given by [34]:

$$\epsilon_s = \frac{C\left(\alpha_s - \alpha_a\right)\Delta T}{1 + \alpha_a \Delta T - C\left(1 + \alpha_s \Delta T\right)} \tag{5.6}$$

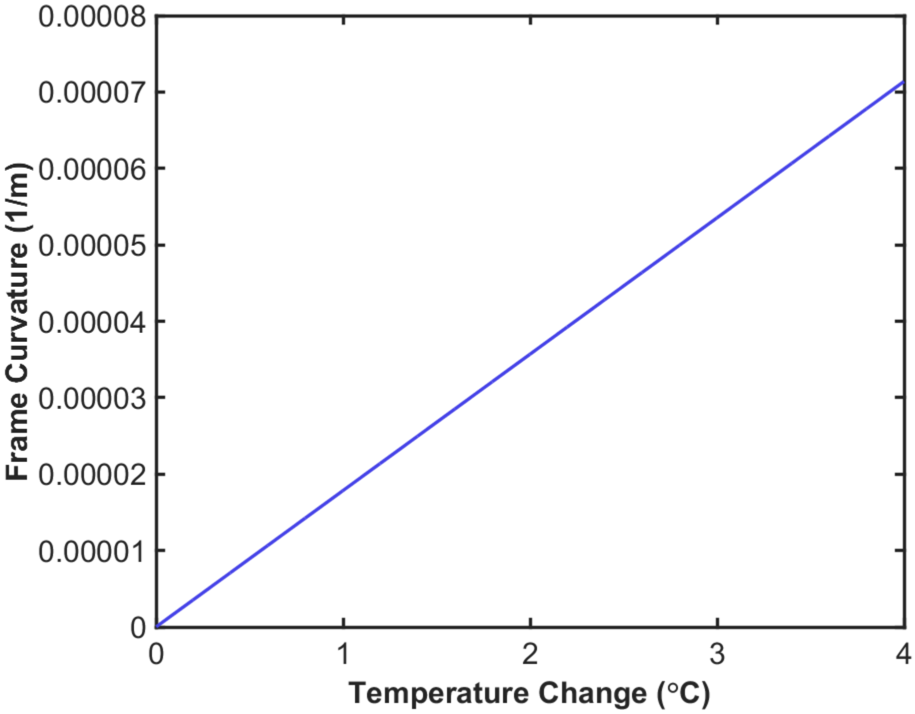

Figure 5-2: Frame curvature due to thermal stress in the film versus temperature change.

$$C = \frac{h_a E_a \left(1 - \nu_s\right)}{h_s E_s \left(1 - \nu_a\right)} \tag{5.7}$$

The subscripts $s$ and $a$ refer to the device properties and the properties of the material being bonded to. The strain in the device is $\epsilon_s$ (m/m) and $C$ is a constant. If the membrane is assumed to experience the same strain as the frame, the integrated stress in the membrane can be approximated as:

$$N_m = \epsilon_s h_m \frac{E}{1 - \nu} \tag{5.8}$$

The difference between the frame expansion and membrane expansion due to temperature change can be accounted for by superposition. Figure 5-3 shows the integrated stress in the membrane the results from a temperature change in a bonded system.

If the device is resting on, and not bonded to, a different material, it will experience

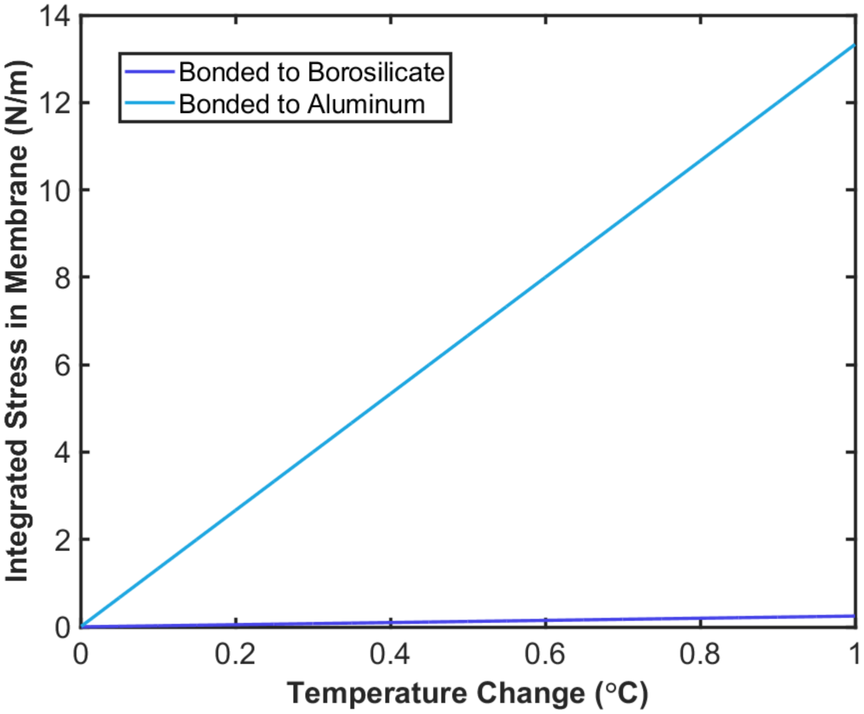

Figure 5-3: Integrated stress in the membrane versus change in temperature for a device bonded to either aluminum or borosilicate. The CTE of aluminum is $2.4\times10^{-}5$ /°C and the CTE of borosilicate is $3.25\times10^{6}$ /°C. The aluminum thickness is 6.35 mm and the borosilicate is 5 mm. The induced integrated stress for a device bonded to borosilicate is 0.025 N/m for a 0.1 °C temperature change.

a frictional force as the material it is sitting upon expands or contracts. The maximum traction force the device would experience is its mass times the forces of gravity times the coefficient of static friction. An Abaqus model, described in the next section, did not show a resonant frequency shift for a coefficient of friction of 1.

# Chapter 6

# Device Mounting

## 6.1 Mounting Forces

### 6.1.1 In-Plane Forces

The circular membrane, which is 2 $\mu$m thick and 3 mm in radius, is etched into a 300 $\mu$m thick silicon frame and cut into a 10 mm by 10 mm square chip. Figure 6-1 shows examples of the device. As the silicon frames are thin, they are subject to in-plane and out-of-plane deformations upon loading. Compressive in-plane forces are particularly undesirable. The membrane will buckle when the tension in the membrane is overcome by a compressive force. A buckled membrane will not adhere to the resonant frequency or deflection modelling detailed previously. Figure 6-1 (c) shows the device buckling under compressive stress.

Finite element analysis performed using Abaqus was done to determine frame bending and membrane buckling under load, as well as the shape of the first resonant mode. The frame was meshed with 100 $\mu$m elements and the membrane was made of shell elements. The model uses C3D8R elements for the frame and S4R elements for the membrane. The membrane is attached to the frame using a shell to solid coupling. Equibiaxial residual stress is added to the membrane with a predefined field. Figure 6-2 shows the ideal first resonant mode shape of the device. The device was modelled with a 5 N/m residual stress that resulted in a 4332 Hz resonant frequency. Equation

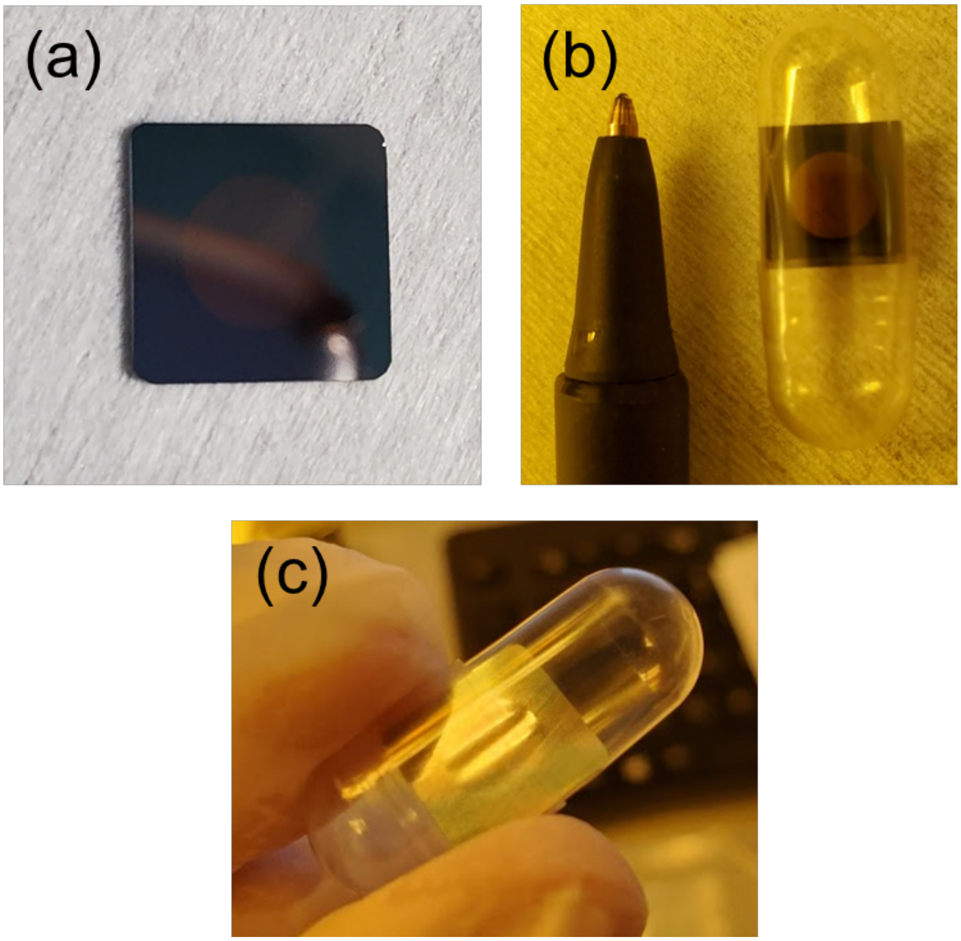

Figure 6-1: (a) Membrane etched into frame sitting on lab wipe. (b) Membrane in protective gel capsule next to ballpoint pen for scale. (c) Membrane buckling under compressive stress when held.

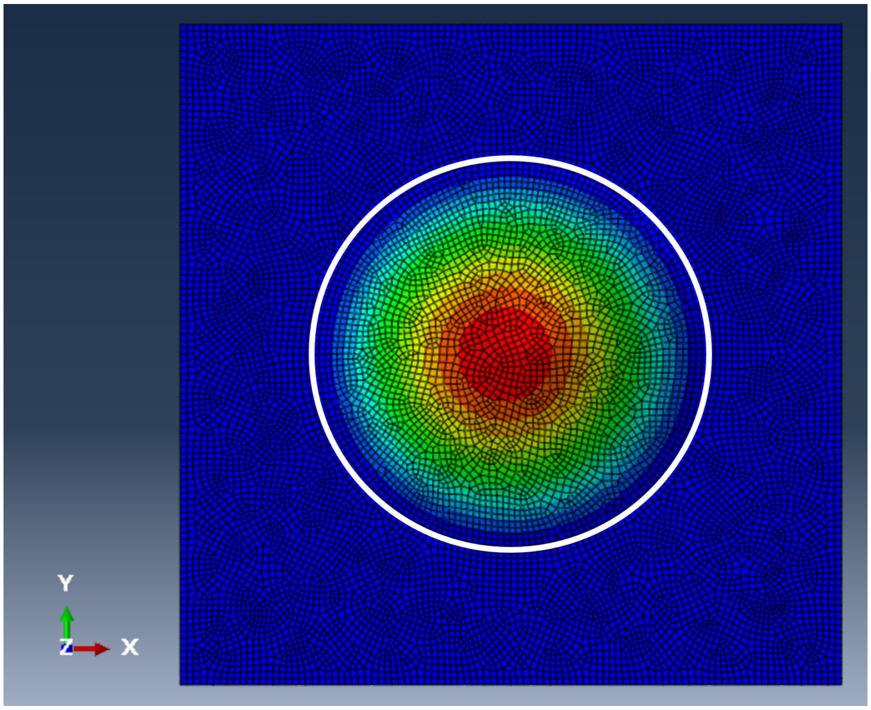

Figure 6-2: First mode shape of the membrane when the bottom and right sides of the frame have the encastre boundary condition (no permitted rotation or displacement) with no loads applied. The resonant frequency is 4332 Hz. Only the membrane moves. Changing the encastre boundary conditions to pinned does not change the resonant frequency. Membrane boundary denoted by white circle.

2.1 predicts a resonance of 4183 Hz. The difference is likely due to stress in the frame that results from the membrane residual stress reaching equilibrium with the frame. The in-plane spring constant for the nominal device parameters is determined to be about 6 N/$\mu$m. Figure 6-3 shows the loading condition used for the analysis. Modelling one side of the frame as a simply supported beam of 2 mm height loaded at midspan gives a stiffness of about 1 N/$\mu$m. Figure 6-4 shows that the membrane does not buckle under a small compressive load of 0.15 N. Under loads as small as 0.7 N, the membrane buckles, as shown in Figure 6-5. The buckled membrane has a different resonant mode and frequency. Figure 6-6 shows the first mode shape at 1261 Hz of a membrane under 1 N load.

While membrane buckling clearly deforms the membrane and invalidates the membrane deformation analysis, small compressive forces still cause problems. In a device with pinned boundary conditions on the bottom and right faces, shown in Figure 6-7,

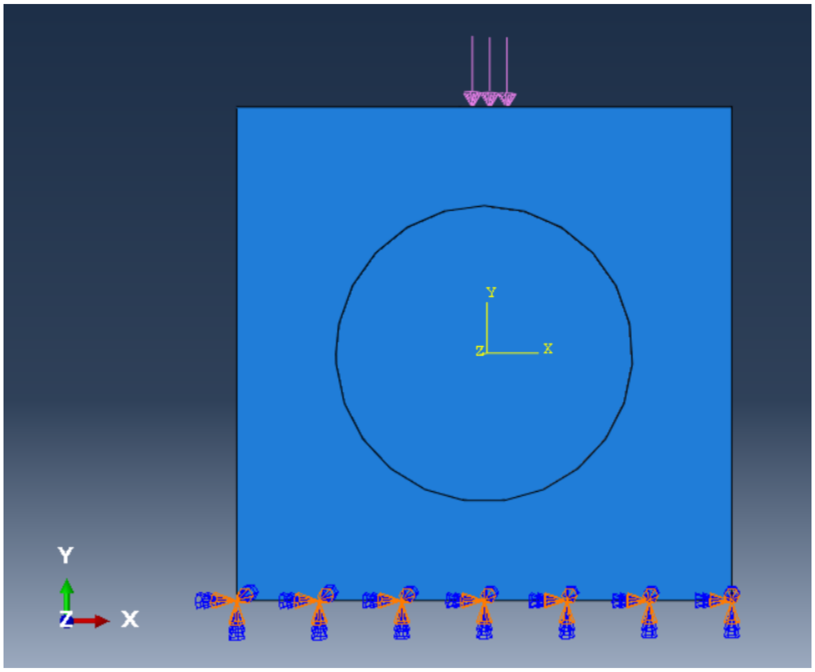

Figure 6-3: Device with in-plane compressive loading. The bottom face is subject to the encastre boundary condition. The top face has a pressure load in the center 1 mm portion.

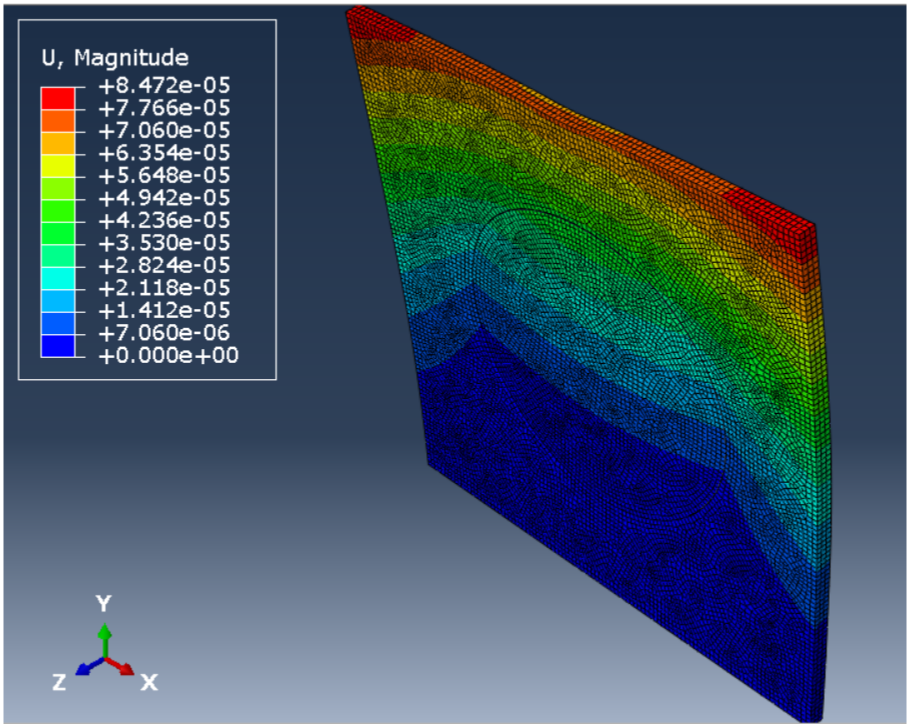

Figure 6-4: Device under 0.15 N compressive force with displacement units in millimeters. The deformation scale factor is 10000 for easy visualization. Due to the residual stress in the membrane, the device bends slightly forwards.

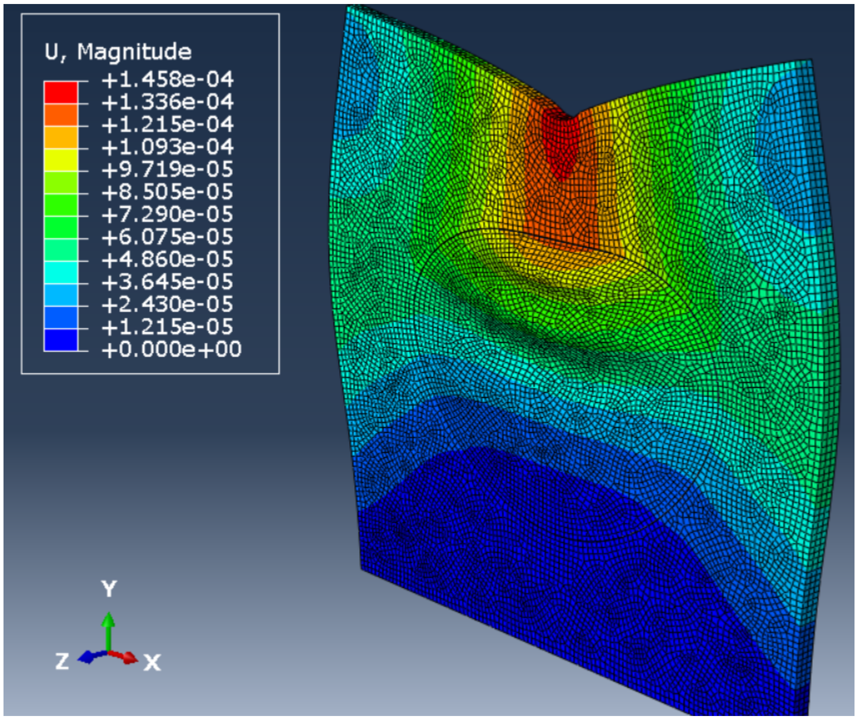

Figure 6-5: Device under 1 N compressive force exhibiting membrane buckling with displacement units in millimeters.

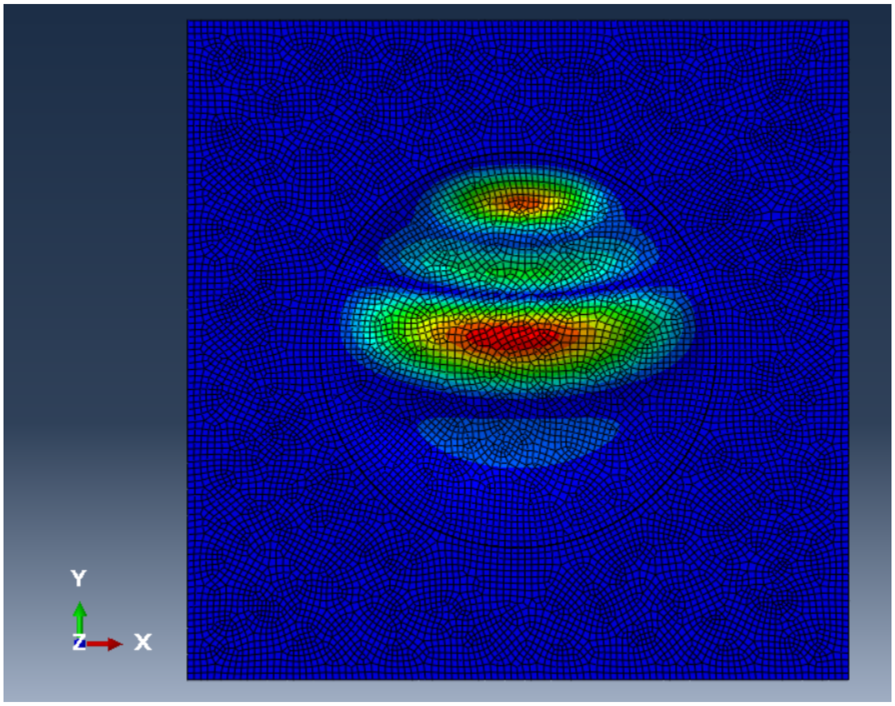

Figure 6-6: First mode shape of buckled device under 1 N compressive force. Resonant frequency is 1261 Hz.

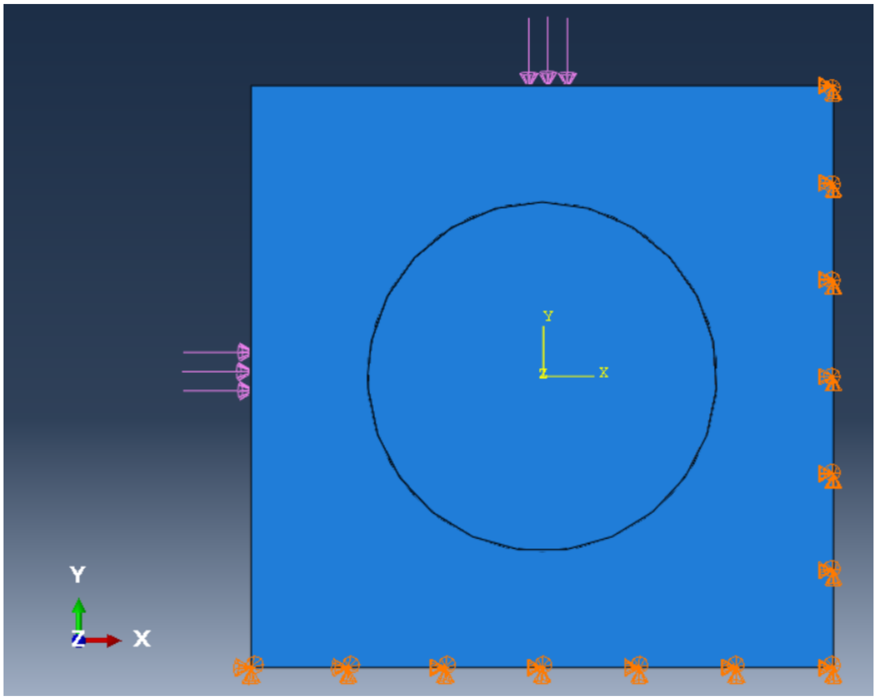

Figure 6-7: Device with pinned boundary conditions on the bottom and right face. Compressive loads are applied over the center 1 mm portion of the top and left faces.

the resonant frequency with no load applied is determined to be 4332 Hz. Loads of 0.005 N applied to the top and left faces over the center 1 mm portion results in a resonant frequency of 4327 Hz, 0.01 N loads result in 4322 Hz, and 0.15 N loads shifts the resonance to 4185 Hz.

The membrane is incredibly sensitive to compressive loads. Using Equation 2.1, a 5 Hz frequency shift to 4327 Hz is a change of 0.012 N/m, a 10 Hz shift to 4322 is 0.025 N/mm, and a 147 Hz shift to 4185 Hz is 0.358 N/m. If the desired repeatability of 0.01 N/m (10% of the maximum allowable stress change of 0.1 N/m) is to be achieved, compressive loads applied in this configuration must change by much less than 0.005 N to accommodate non-repeatability from other sources such as temperature fluctuation.

### 6.1.2 Out-of-Plane Forces

Forces that induce bending in the silicon frame can cause stress changes in the membrane. Concave down bending results in a tensile stress in the membrane while

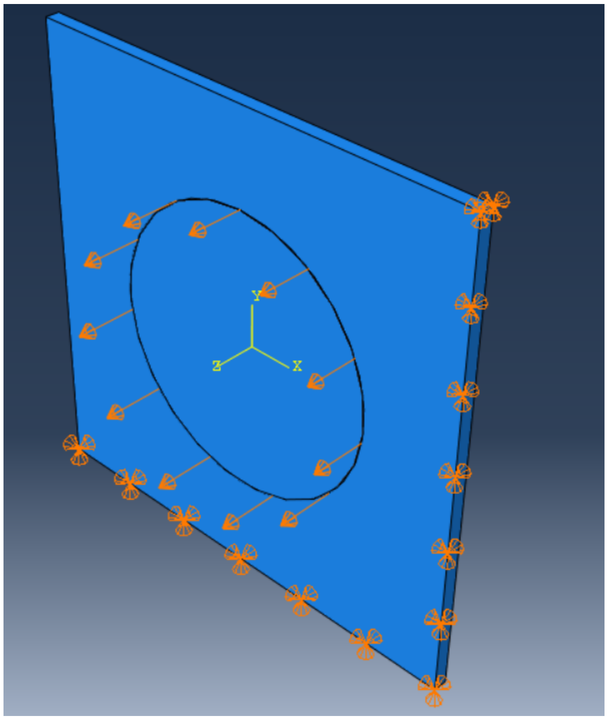

Figure 6-8: Device with frame pinned on the bottom and right faces with a prescribed displacement along the outside of the membrane used to determine resonance change from radius of curvature changes.

concave up bending results in a compressive stress. Finite element modelling was used to determine resonant frequency change given a radius of curvature. Figure 6-8 shows the boundary conditions used for the analysis. A displacement of the outside portion of the membrane given a radius of curvature of frame bending was calculated and used in the model as a prescribed displacement. The simulated first resonance of the membrane was used in equation 2.1 to calculate the integrated stress change compared to an unbent model. A small radius of curvature of 20 m produced 3.9 N/m of integrated stress in the membrane. Radii of curvature above 10,000 m had an asymptote of 0.06 N/m. As these radii of curvature are associated with displacements of less than $8 \times 10^{-7}$ mm, it is possible that this asymptote is due to modelling limitations. Bending due to temperature changes of less than 1 °C in coated devices produces radii of curvatures around 100,000 m or greater. It is likely that this curvature results in a negligible integrated stress change. The model is also limited in accuracy as it only approximates the curved shape.

## 6.2 Mount Design

### 6.2.1 First Method

The device's resonant frequency is sensitive to many factors, including actuation force, compressive forces, temperature change, atmospheric pressure, and bonding material. To make a repeatable resonant frequency measuring tool, the device needs to be mounted in a way that minimizes non-repeatability due to temperature fluctuations and forces acting on the membrane's silicon frame imparted during mounting. Three different approaches were tried. The devices are tested with uncoated membranes. A swept sine voltage electrostatically actuates the membrane. Displacement is recorded to find the resonant frequency.

The first method was done in air and displacement is measured with the MTI-2100 Fotonic sensor with 2125CTI probe, a fiber-optic displacement sensor with 0.178 m/mV sensitivity and 0.762 mm standoff distance [79]. The silicon device was positioned using a 3-2-1 arrangement without preload [80,81]. It sits on three 1/16 inch diameter ball bearings and rest against three cylindrical protrusions waterjet in 1/4 inch 6061 aluminum. The electrode is 6mm diameter copper rod that can be adjusted vertically with a fine adjustment screw to control the separation between the electrodes. Actuation voltages of 15 V and larger were used. Figure 6-9 shows the CAD model of the device and its parts. Figure 6-10 shows the device with sensor.

The Fotonic sensor was positioned above the device with a micrometer stage positioning arm from MTI. The sensor illuminated the entire membrane. The device was grounded through side contact with grounded aluminum. Figure 6-11 shows the proof of concept results obtained with this mounting design where change in DC voltage was used to simulate an integrated stress change in the membrane.

The displacement between the membrane and bottom electrode in this setup was hard to determine as there was no initial setpoint. The electrode was moved upward until slight distortion could be seen in the membrane's flatness and then the electrode was backed off. The membrane would frequently be deformed either with slight wrinkles or holes from this alignment procedure. Additionally, positioning the device

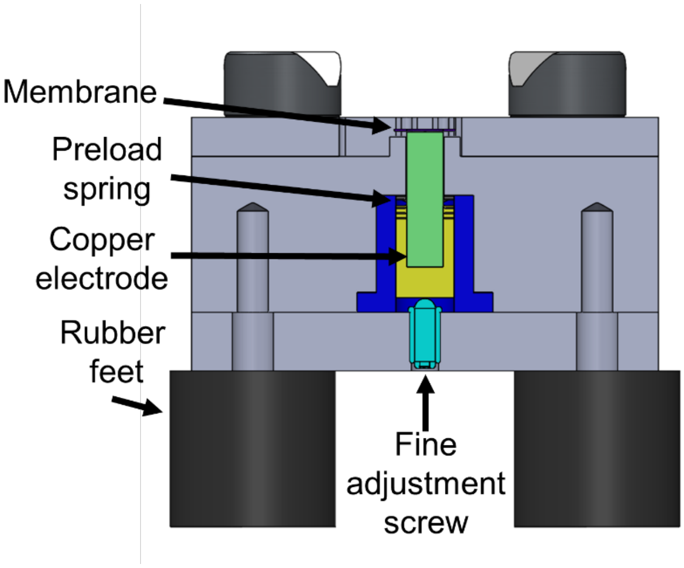

Figure 6-9: CAD model of first design for device mounting. The device sits on ball bearings and the electrode is positioned with a fine adjustment screw. Rubber feet help damp vibrations.

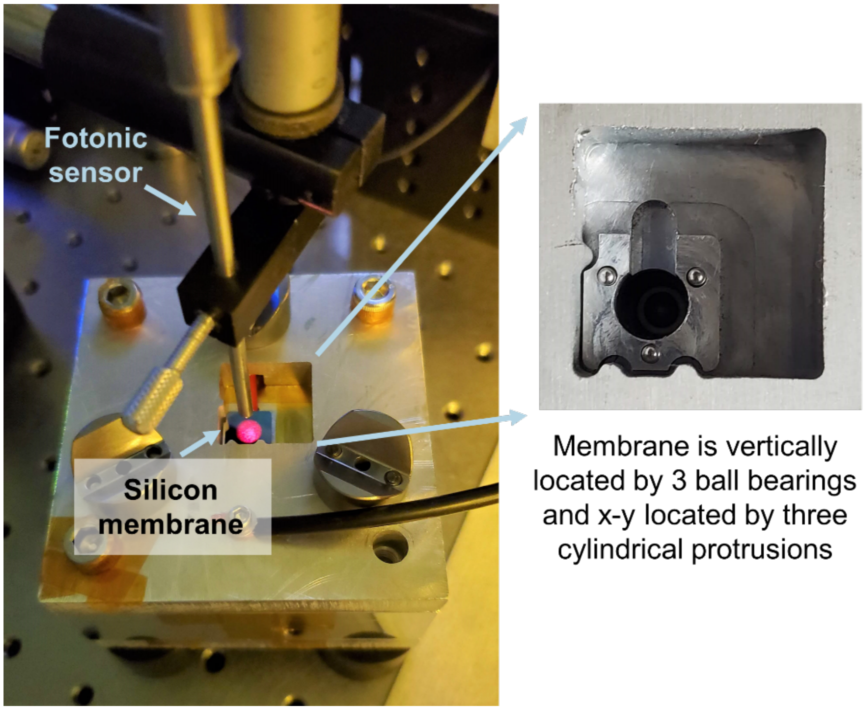

Membrane is vertically located by 3 ball bearings and x-y located by three cylindrical protrusions

Figure 6-10: Device being tested in first mounting design. Details of the 3-2-1 device positioning setup are shown.

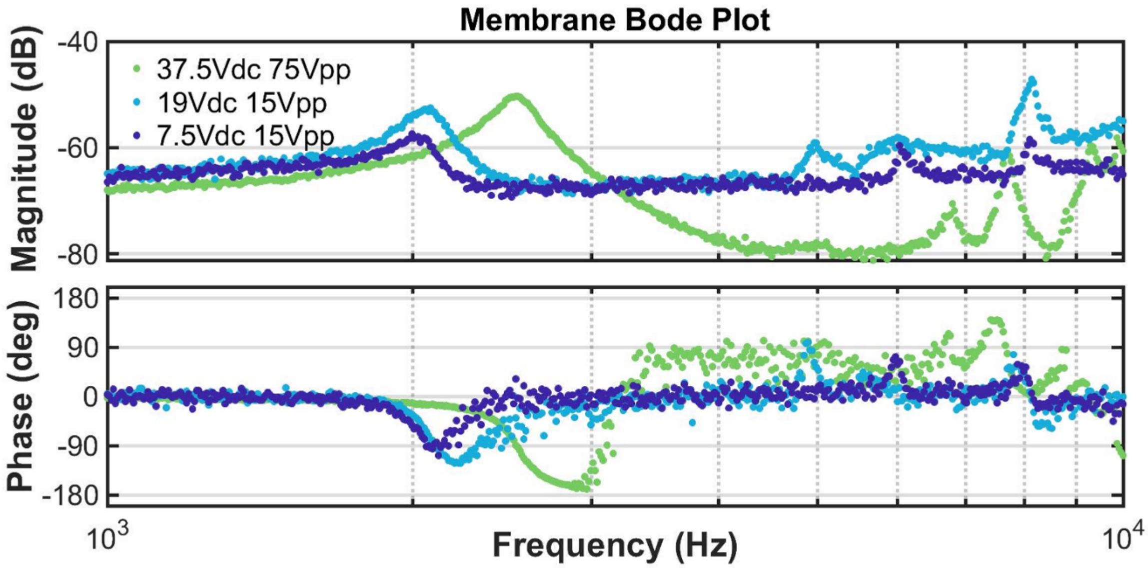

Figure 6-11: Preliminary swept sine frequency sweeps for the first mounting method. Actuation voltage was increased to artificially change the integrated stress of the membrane. The about 40 Hz difference between the actuation voltages of 7.5 V DC and 19 V DC corresponds to a 0.1 N/m integrated stress change when air damping is accounted for.

with tweezers was especially difficult. The membrane would tear it was accidentally touched or if the device fell membrane side down.

### 6.2.2 Second Method

The second mounting method, shown in Figure 6-12, was for vacuum down to about 500 mTorr to reduce the effect of air damping. The membrane was also clamped between two lapped aluminum plates to make handling easier. The clamp is kinematically positioned above the bottom electrode. The electrode height is controlled by a fine adjustment screw. The MTI Fotonic sensor was fed through the acrylic vacuum lid as shown in Figure 6-13. The acrylic lid would bend under vacuum and the sensor had to be carefully positioned so it did not pierce the membrane as vacuum was drawn. The resonant frequency measurements shifted by around 600 Hz, centered around 7240 Hz, likely due to temperature effects from the aluminum clamp (discussed in Figure 16). The clamp could be made of material CTE matched to silicon to decrease the effects of temperature fluctuations. However, adjusting the height

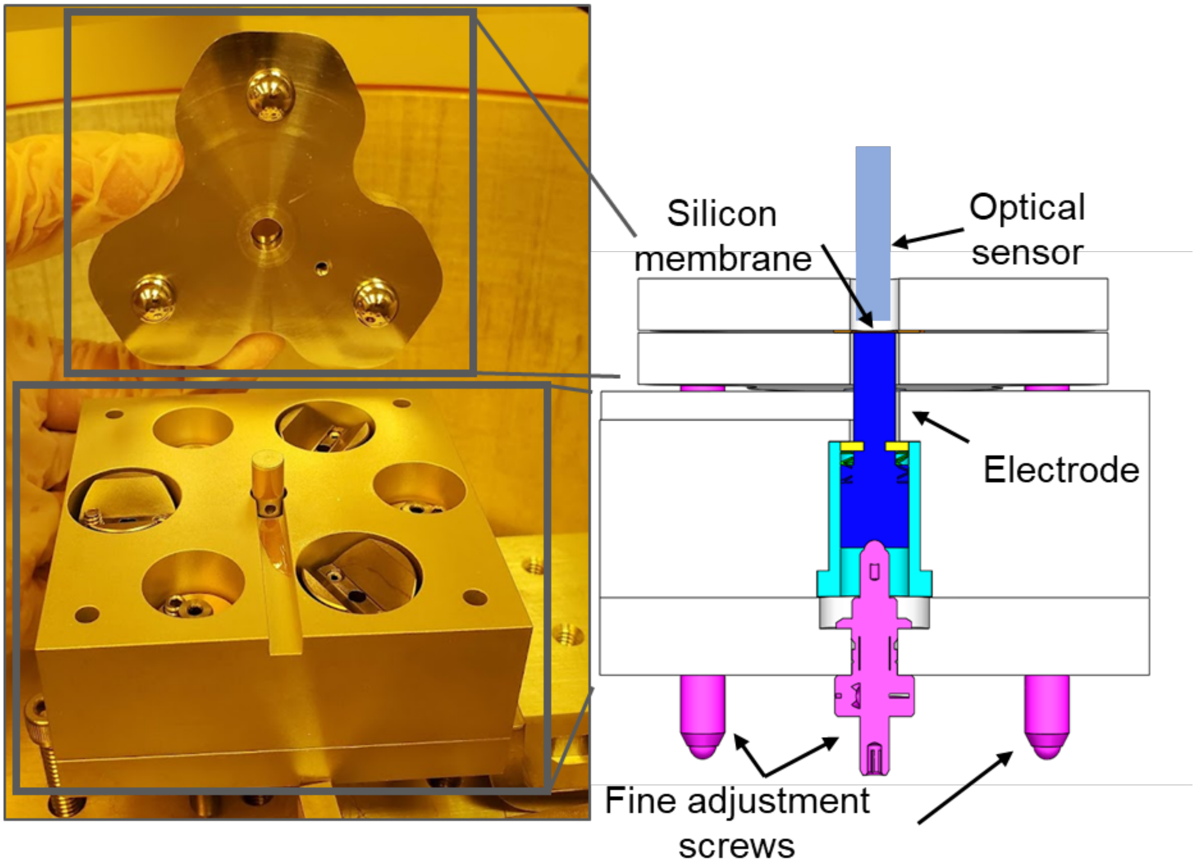

Figure 6-12: Second mount design with labelled components. The membrane is clamped between two lapped aluminum plates. The bottom plate kinematically connects to the mount base that has the bottom electrode. The electrode is moved with a fine adjustment screw. The whole mount sits on three fine adjustment screws that control tilt, tip, and height of the mount. The optical sensor goes through the upper aluminum plate to measure the membrane.

of the bottom electrode was hard to calibrate and resulted in membrane tearing.

### 6.2.3 Third Method

The third mounting method was in vacuum of less than $10^{-5}$ Torr to eliminate the effects of air damping. The mount fits inside a vacuum flange cross through an access door. The flange outer diameter is 4.5 in. Membrane displacement is measured through a viewport with a laser doppler vibrometer (LDV). The LDV is the VibroGO from Polytec. It has a bandwidth of 25 kHz and has a resolution of 16.95 pm [82].

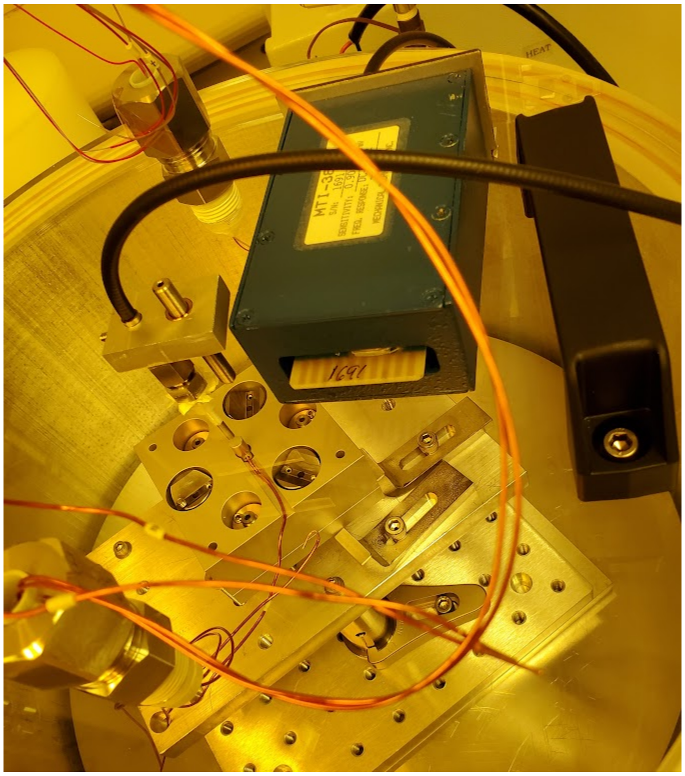

Figure 6-13: Second mount design in vacuum chamber. The chamber has a clear acrylic lid through which the MTI Fotonic sensor is fed through. Sensor height is controlled with a fine adjustment screw.

The LDV is mounted on a custom tip and tilt platform that has fine adjustment screws.

The device, shown in Figure 6-14, is fixtured on a special borosilicate glass holder which is then fixtured inside a vacuum flange. Borosilicate is close in CTE to silicon and minimizes thermal stresses. The borosilicate glass holder allows electrical connection to the membrane and electrode. It is a two-part design, comprised of a 500 $\mu$m thick, 25.4 mm square borosilicate glass wafer and 5 mm thick borosilicate glass blank fabricated by waterjetting. Conductive silver adhesive, Product No. 16062 from PELCO, bonds the two pieces together and creates electrical traces that run off the side of the glass blank. The first layer of the adhesive is specified by PELCO to be about 25 $\mu$m thick. A 178 $\mu$m thick, 5.9 mm diameter steel circle cut from shim stock acts as the electrode and is adhered to the glass wafer with the silver adhesive. The silicon frame sits completely on borosilicate glass. The electrode with adhesive is about 100 $\mu$m from the membrane, with variability due to adhesive painting and steel stock tolerance. The glass holder is shown in Figure 6-15 along with an example of waterjet fixturing.

The borosilicate glass holder is held in the vacuum chamber by means of a kinematic holder. A view of the device in the chamber is shown in Figure 6-16. It sits on three borosilicate glass balls and is positioned against three ceramic posts. Two of the posts are coated with silver adhesive and form an electrical connection with the traces on the glass holder. A flexure provides preload to keep the glass holder in contact with the posts used for the electrical connection. The preload is designed with enough axial stiffness and high enough critical buckling load to overcome the frictional forces acting on the glass holder. The kinematic holder freely sits in the flange on three steel hemispheres.

The glass holder is an improvement upon the other mounting designs. The chances for membrane damage are minimized by the fixed electrode separation and indirect handling of the silicon device. Additionally, the borosilicate glass is closely matched to silicon in CTE, minimizing stress changes due to temperature fluctuations. Forces from placing the glass holder in the kinematic mount are borne by the glass, reducing

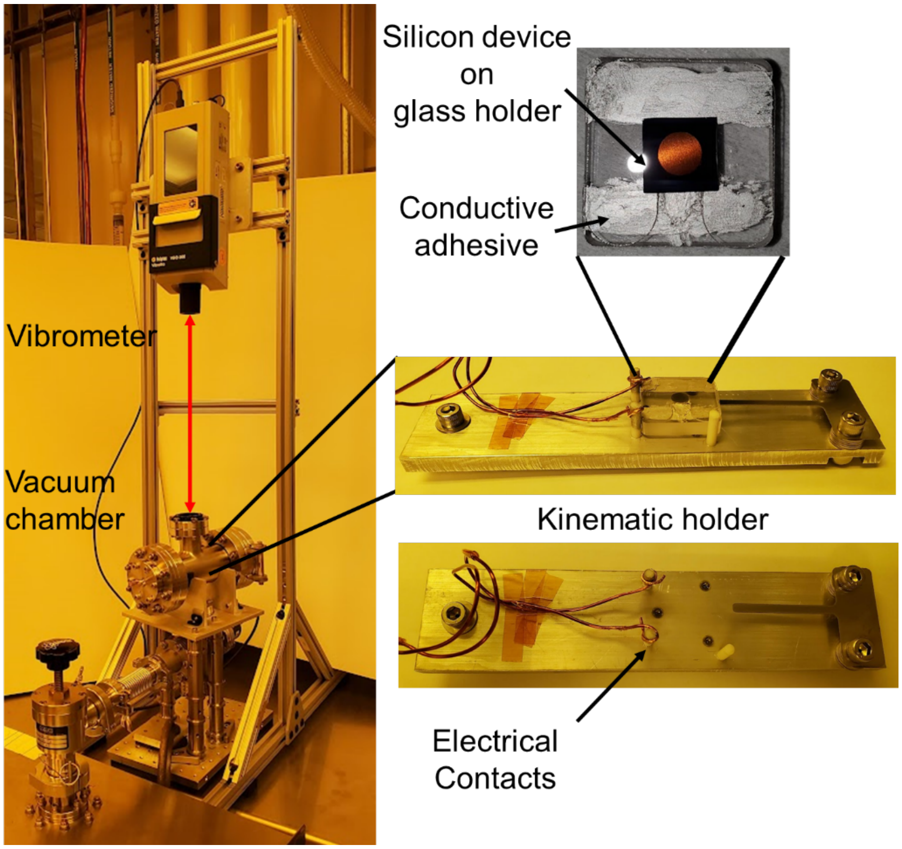

Figure 6-14: Third mount design. The kinematic holder fits inside a vacuum flange. Membrane displacement is measured optically through a viewport with a Laser Doppler Vibrometer. The device sits on a CTE matched glass holder that has an electrode and electrical contacts that connect to the kinematic holder. The glass holder sits on three glass spheres.

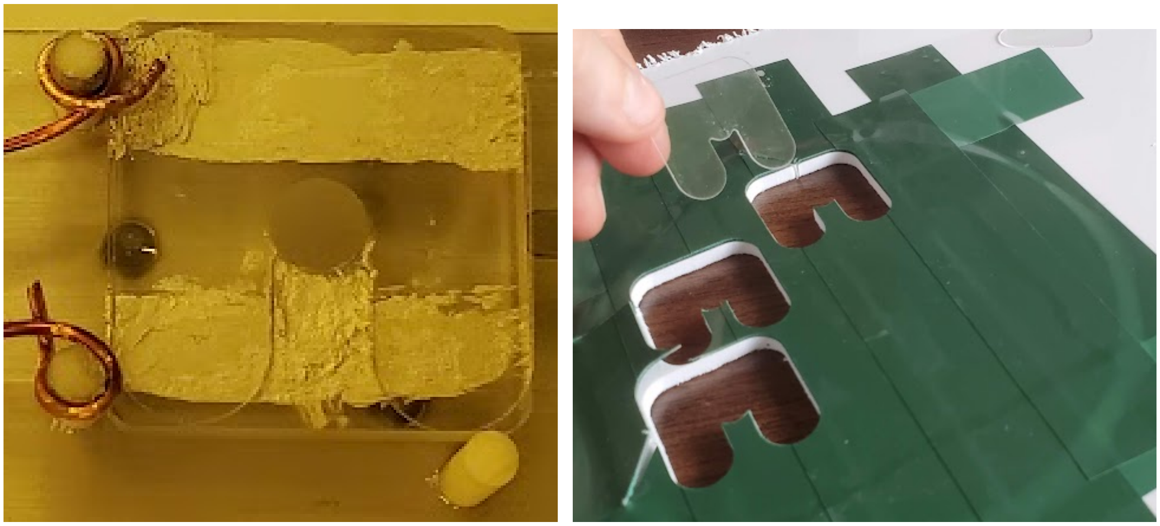

Figure 6-15: (Left) Glass holder showing the glass wafer, glass blank, steel electrode, and silver conductive adhesive traces. The three ceramic posts position the glass holder with preload from a flexure. The ceramic two posts on the left are coated with conductive adhesive, which make electrical contact to the glass holder. Wire wraps around the posts to supply voltage to the setup. The total resistance of each path is a few Ohms. (Right) Waterjetting setup for the glass wafer. The wafer is taped on sacrificial plastic sheet. The waterjet pierces the plastic and then cuts into the wafer.

resonant frequency shifts. An Abaqus simulation was done to determine the resonant shift from loads on the glass holder. The bottom of the device frame was tied to the glass holder top, meaning that there is no relative motion between the two surfaces. This constraint would represent the device bonded to the glass such as what happens when anodic bonding is used. Figure 6-17 shows the loading and boundary conditions used. The simulation predicted a 0.005 N/m stress change for loads of 0.05 N applied to the top and side of the glass, a 0.010 N/m shift for 0.1 N loads, and a 0.098 N/m shift for 1 N loads. Compared to the device alone, this configuration is about 20 times less sensitive to applied compressive loads. Since the device and glass are not bonded together and relative motion creates frictional forces only, the device should be even less sensitive to loads applied to the glass holder.

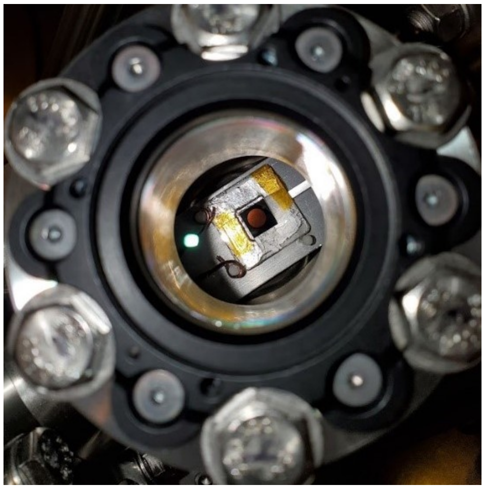

Figure 6-16: Device and mount seen through the chamber viewport. Indium solder ribbon of 0.002 inch thickness is used to ground the electrode as well as keep it in place on the glass holder.

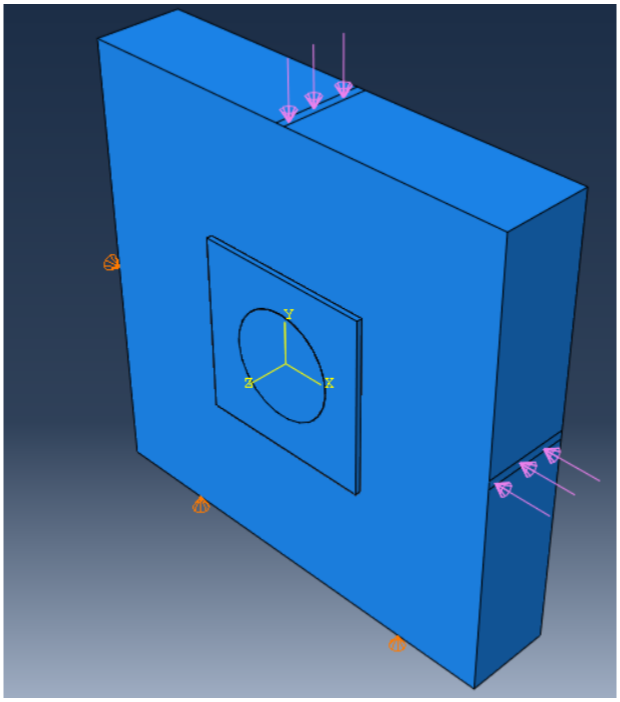

Figure 6-17: Abaqus model for determining resonance shift from loads applied on glass holder. The loads are the purple arrows. The orange arrows on the left prevent displacement in the x directions while the orange arrows at the bottom prevent displacement in the y direction (representing the ceramic posts). On the backside, not shown, three points prevent displacement in the z direction. The Young's modulus of the glass used was 64 GPa and the Poisson's ratio was 0.2.

# Chapter 7

# Experimental Results

## 7.1 Resonance Testing

The third mounting method was used and the membrane was actuated with a swept sine voltage with a 0.5 V DC voltage and 0.5 V peak-peak AC voltage from a SIGLENT SDG1025 waveform generator. The tests were done under vacuum of less than $10^{-}5$ Torr. The membrane was kept at each frequency for 5 seconds with at least 10 frequencies in each sweep. The measurement, sampled at 100,000 Hz, was high pass filtered with a passband of 1000 Hz. The displacement magnitude and phase in volts of the resonance was taken from an FFT of the filtered signal. The input signal's magnitude in volts and phase was also obtained by FFT. The data was recorded with a National Instruments CompactDAQ NI-9205 board.

The setup was sitting in lab air and subject to the lab's temperature fluctuations of 2 °C. Impulse testing, performed by tapping the chamber and recording the membrane vibrations, gives a preliminary resonant frequency around which to perform the swept sine. Figure 7-1 shows an impulse test. The first resonance and the second harmonic are shown. The low frequency resonances are likely resonances in the structure. Over a week of testing, the average measured stress was 8.227 ± 0.008 N/m. A month of being stored in lab air later, over three days of testing, the average measured stress was 8.214 ± 0.006 N/m. The standard deviation of the mean is calculated to 95% confidence interval, i.e. the standard deviation times a t-factor divided by the square

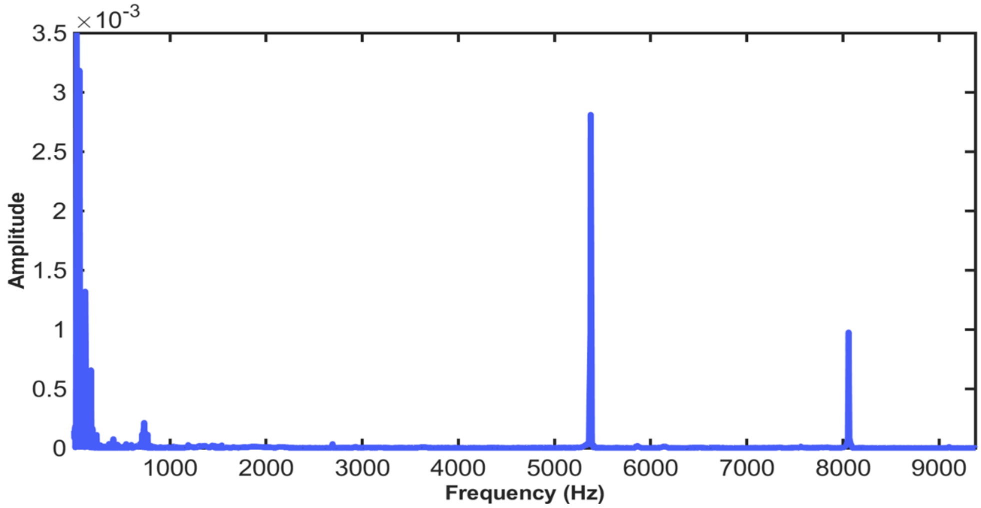

Figure 7-1: Impulse testing on membrane in chamber. The chamber is tapped, the response is measured by the LDV, and a fast Fourier transform (FFT) is performed to find the resonances. The graph shows the first resonance of the membrane, around 5370 Hz and the second resonance at around 8000 Hz. The low frequency resonances are likely structural resonances of the mount and chamber.

root of the number of samples, and is taken as the repeatability in this thesis. Figure 7-2 shows a typical bode plot for the membrane. The device was not moved from the chamber during these tests and was held at atmospheric pressure. The functional requirement of the device is a 0.01 N/m repeatability when removed from the chamber and placed back in multiple times. Temperature fluctuations were assumed to be the main cause of non-repeatability.

### 7.1.1 Temperature Controlled Enclosure

The whole setup was moved into a temperature-controlled environment. The control algorithm and one temperature control unit (of two) that Zhao et al. describe was used for the environment [83]. The temperature-controlled environment is made of foam board insulation and encloses a vibration-isolated optical table. The air temperature inside the environment near the setup is plotted in Figures 7-3 and 7-4. Turning on the electronics increases the air temperature locally near the control thermistor but not for the rest of the environment, causing the air temperature to drop and reach a new equilibrium. Measurements were taken once the air temperature settled to

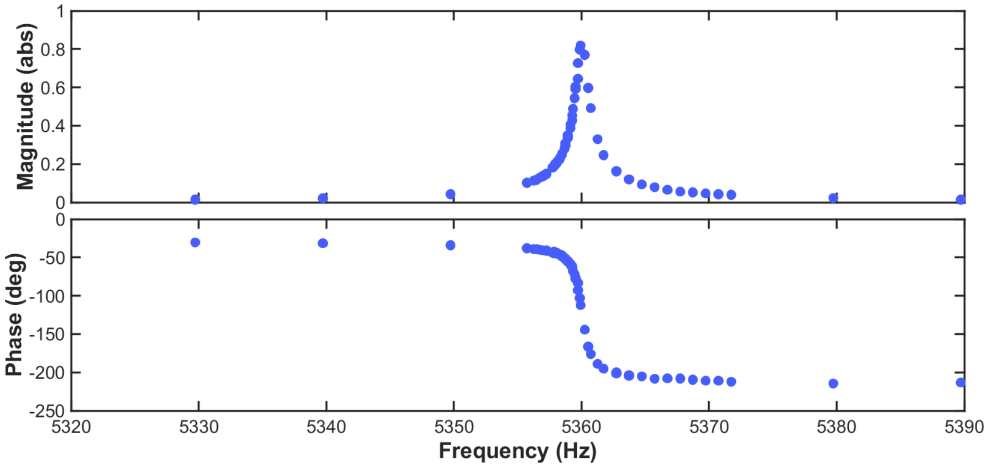

Figure 7-2: Example of resonant test done on uncoated membrane to measure repeatability. The membrane is actuated with a 0.25 V swept sinusoid with a 0.5 V DC offset. Over a week of testing, the average measured stress was 8.227 ± 0.008 N/m. A month later, over three days of testing, the average measured stress was 8.214 ± 0.006 N/m. Mean standard deviations are reported to the 95% confidence interval.

the new equilibrium. The figures represent the temperature during a typical day of testing with power cycling of the electronics. The temperature was 20.843 ± 0.013 °C. A K type thermocouple was also placed inside the vacuum flange, however the sensitivity of 0.02 °C obscured any valuable data. A dunking analysis using lumped capacitance, as the Biot number of the membrane is small, where the membrane is subject to black body radiation from the chamber walls shows that the membrane's temperature will reach the temperature of the chamber walls in about 15 seconds.

### 7.1.2 Laser Heating

The membrane is also sensitive to laser heating. The $<$ 2 mW laser is focused on the membrane creating a spot size of less than 1 mm. Figure 7-5 shows the effects of placing an absorptive neutral density filter on the viewport window to reduce the power of the laser. The resonant frequency of the membrane increases with increasing filter optical density. The laser likely heats the membrane and causes it to expand relative to the frame, reducing its tension. Resonant frequency shifts created by laser power changes was observed in resonant micro-cantilevers by Sadeghian et al [84]. A filter with 3 O.D. was added to the setup for all subsequent tests. When the laser is kept on and a frequency sweep is done every four minutes for four hours, the membrane resonance slowly increases, as shown in Figure 7-6. If the membrane were the only object being heated, the resonance should decrease as it expanded. The increase in frequency is likely due to the whole glass holder, which has a higher CTE than silicon, being heated. Some of the laser power transmits through the silicon membrane and is partially absorbed by the steel electrode. The heat from the electrode conducts through the conductive adhesive into the glass. The resonant frequency drift upwards continued for several days until an equilibrium was reached. However, as sweeps last less than four minutes, effects from laser heating of the entire holder should be negligible.

The sweeps for the 3 O.D. filter in Figure 7-5, shown again in Figure 7-7, were each fit to a double Gaussian of the form, $y = a_1 \exp(-((x-b_1)/c_1)^2) + a_2 \exp(-((x-b_2)/c_2)^2)$ using the Levenberg–Marquardt algorithm in MATLAB. An example fit is shown in Figure 7-8. It has an $R^2$ value of 0.9993 and a root mean square error of 0.0016. The mean resonant frequency of all the sweeps was found to be $5.367 \times 10^3 \pm 0.894$ Hz with a mean integrated stress of $8.230 \pm 0.003$ N/m. Moving the setup to the temperature-controlled chamber and filtering the laser greatly improved the repeatability of the measurements. As the target repeatability is 0.01 N/m, there is now buffer for the non-repeatability due to remounting the glass holder.

### Mounting Repeatability Testing

Preliminary testing for integrated stress repeatability when the glass holder is taken out of the vacuum chamber and remounted was performed. Four different trials were done. The membrane was measured on the first trial and then remounted on each subsequent trial. After fitting, the mean resonant frequency was $5.382 \times 10^3 \pm 11.194$ Hz and the mean integrated stress was $8.275 \pm 0.034$ N/m. The added non-repeatability is believed to be dominated by changing the laser position on the membrane. Tilting of the silicon device was also investigated as a cause of non-

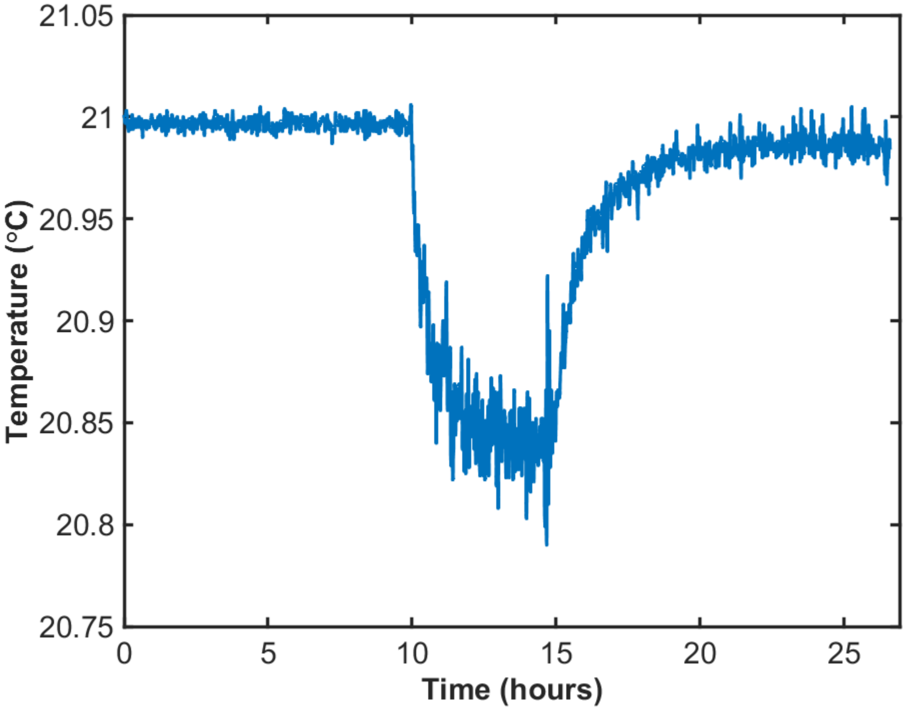

Figure 7-3: Air temperature inside the thermally controlled environment versus time in hours. The temperature is measured near the vacuum flange that holds the device. Around hour 10, the LDV and signal generator were turned on, generating heat. The electronics are close to the control thermistor so the temperature is lower farther away from the electronics. At hour 15 the electronics are turned off and the temperature increases.

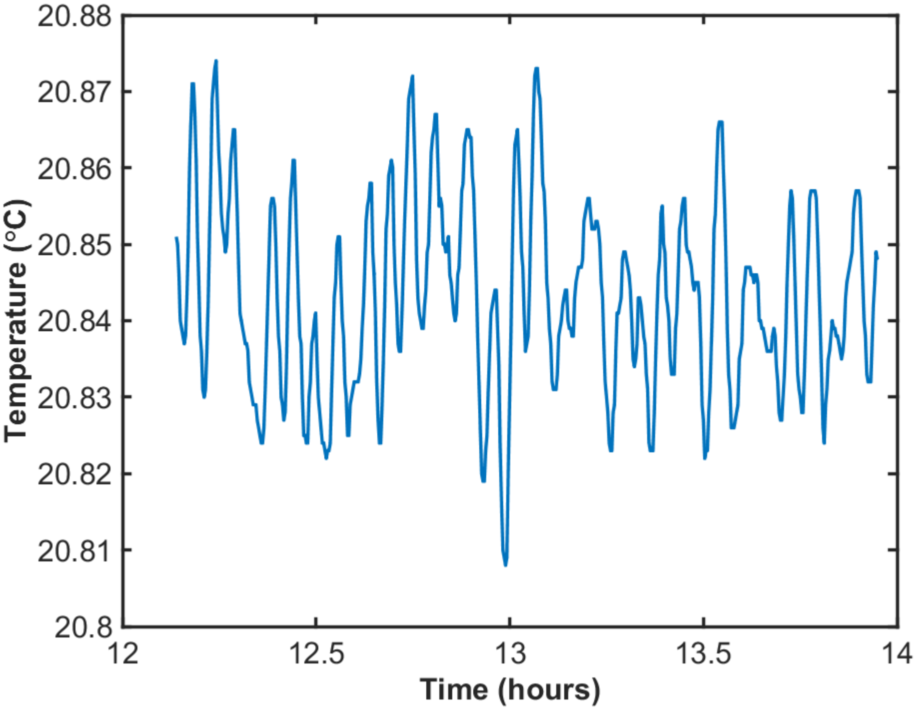

Figure 7-4: Air temperature in temperature-controlled environment versus time. The temperature was measured near the flange that hold the device. The temperature is 20.843 ± 0.013 °C over the two hour period, hours 12 to 14 from Figure 7-3.

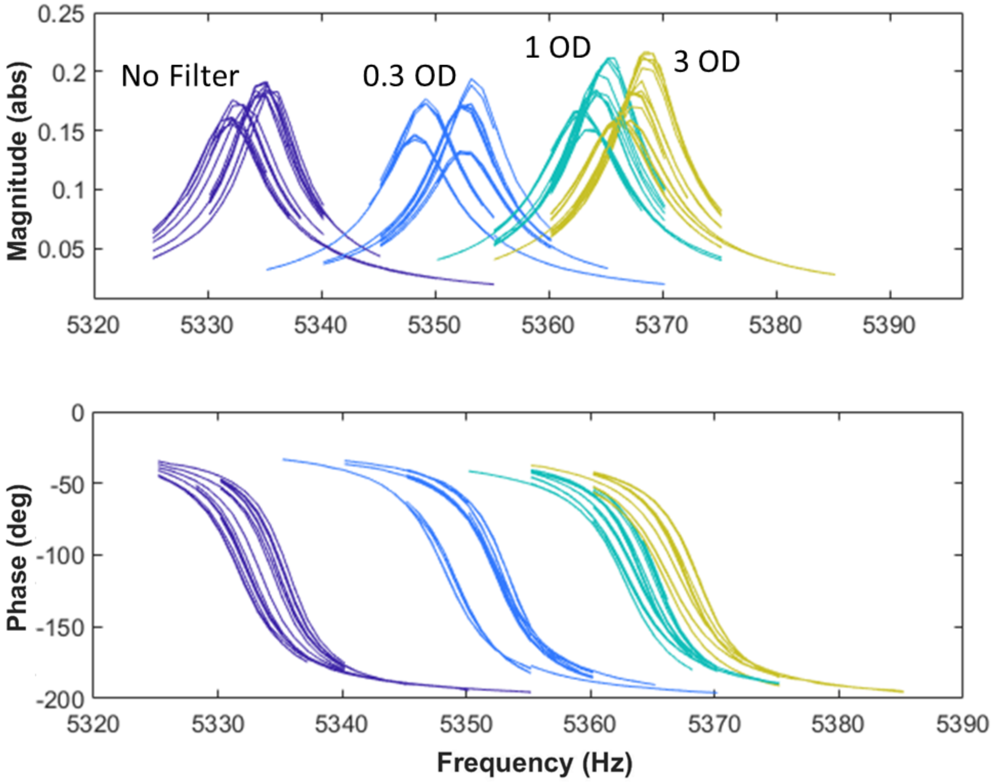

Figure 7-5: Bode plots of an uncoated membrane. Three sweeps were taken on six days over an eight-day period. On each day, three membrane sweeps each for three different neutral density filters and no filter were performed under vacuum. The filters had optical densities of 0.3, 1, and 3. The corresponding sweeps are labelled. The device remained in the chamber at atmospheric pressure between trials.

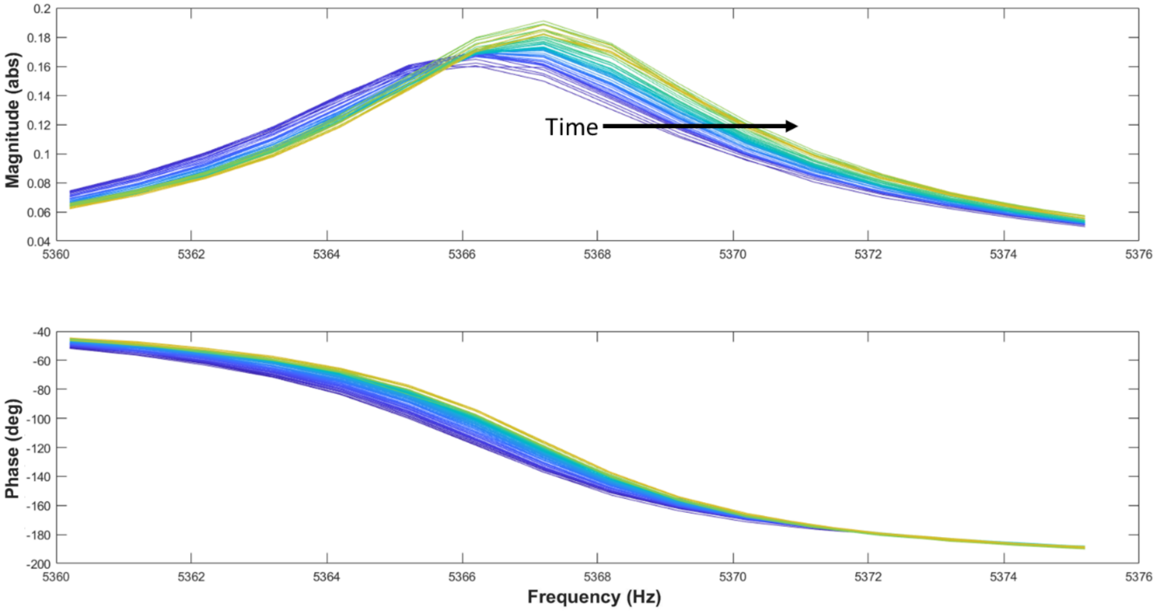

Figure 7-6: Frequency sweeps taken every four minutes over a four-hour period. The resonance slowly increases. The increase in integrated stress is thought to be from laser heating of the entire glass holder, which expands faster than silicon.

repeatability, but was found to be insignificant through experimental testing and simulation in Abaqus. The kinematic holder is not fixtured to the flange and is free to move. An experiment where the laser position was moved around the membrane while the membrane remained in the chamber under vacuum was performed. The positions are the center of the membrane and then a square grid with the laser about halfway between the center and edge of the membrane. Figure 7-9 shows the experiment. The mean resonant frequency was $5.364 \times 10^3 \pm 11.993$ Hz and the mean integrated stress was $8.220 \pm 0.037$ N/m. The laser may heat up the membrane nonuniformly and slightly shift the mode shape. This issue can be prevented if the kinematic holder is fixtured inside the vacuum chamber.

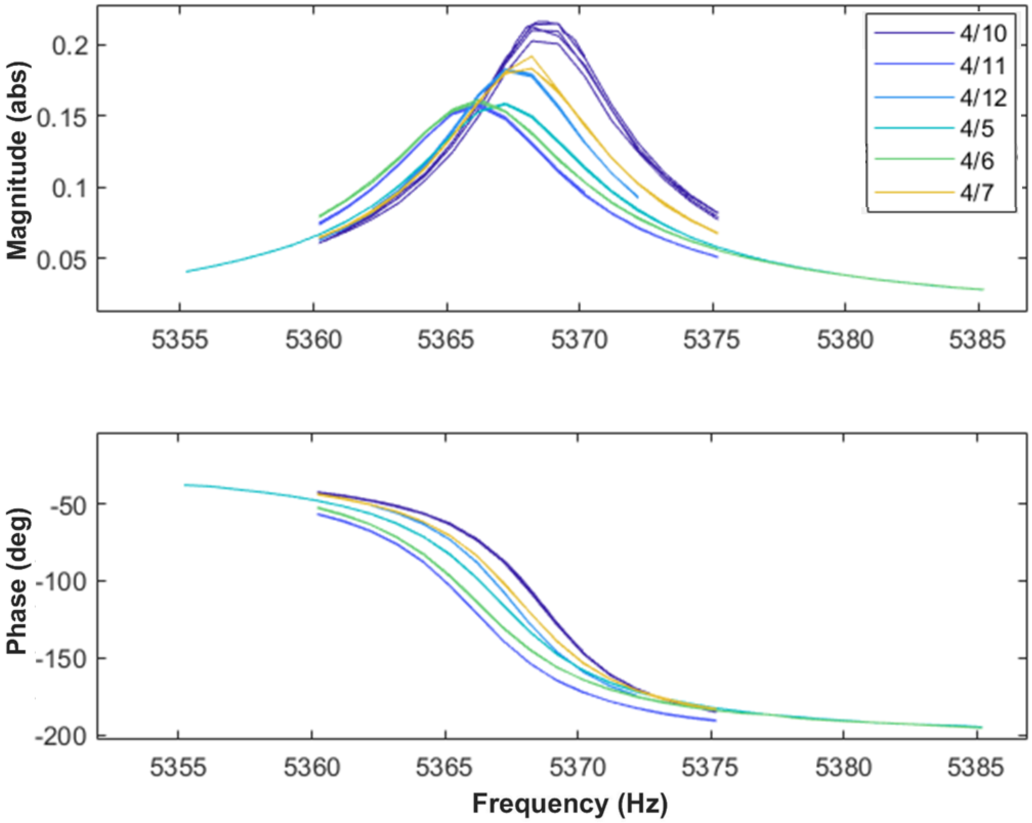

Figure 7-7: Frequency sweeps using the 3 O.D. filter. The uncoated device was kept in the vacuum flange at atmospheric pressure between trials. The resonances dither back-and-forth every day and don't appear to have a trend.

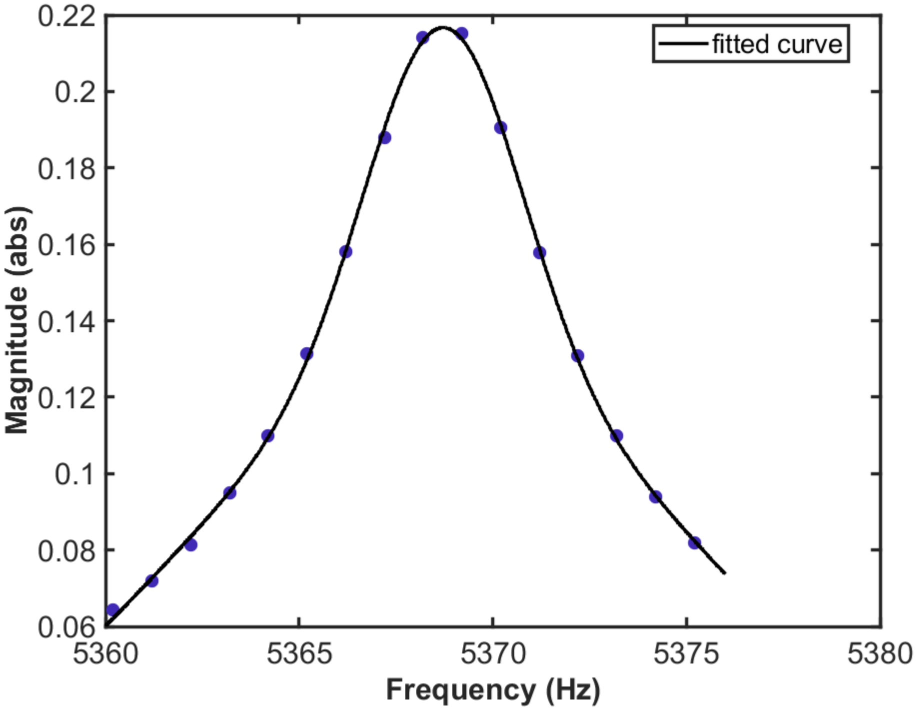

Figure 7-8: Sample fit of a singular frequency sweep from Figure 7-7 using the Levenberg–Marquardt algorithm. It has an $R^2$ value of 0.9993 and a root mean square error of 0.0016. The mean resonant frequency of all the frequency sweeps, fitted individually, was found to be $5.367\times10^3\pm$ 0.894 Hz with a mean integrated stress of $8.230 \pm 0.003$ N/m.

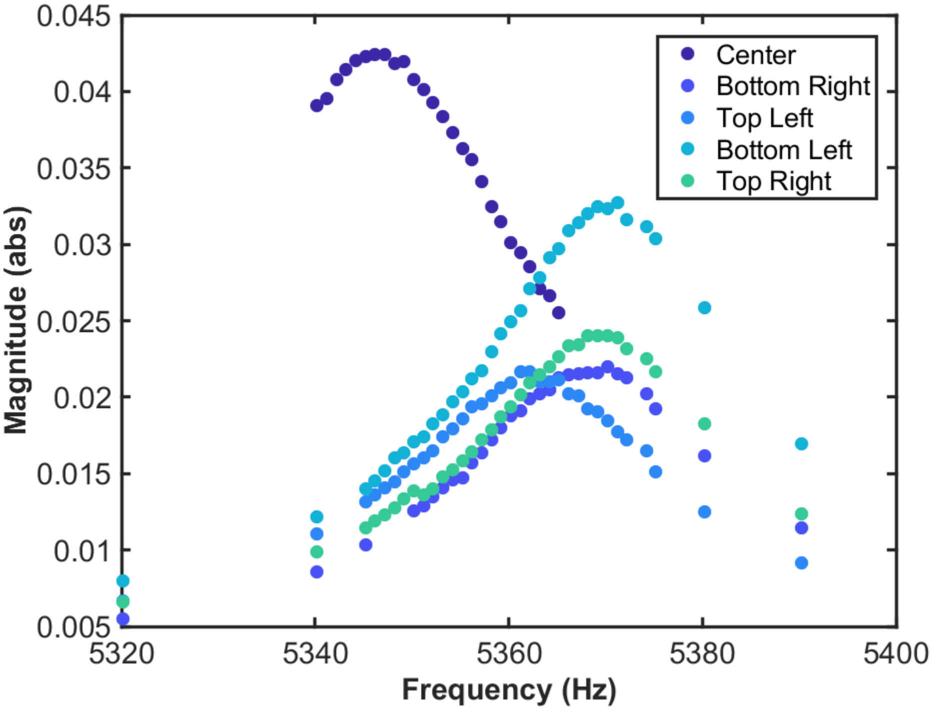

Figure 7-9: Frequency sweeps where the membrane stays in the chamber under vacuum and the laser spot is moved to different positions. The mean integrated stress was 8.220 ± 0.037 N/m.

# Chapter 8

# Conclusions and Future Work

The membrane resonance technique for measuring stress in thin films has proven to be useful for measuring integrated stress development in thin films during deposition. This thesis extends the technique's capability to measuring integrated stress stability over time for already deposited films with repeatability suitable for use choosing reflective coatings for the next great X-ray observatory.

The membrane resonance technique is highly sensitive to changes in integrated stress and is well suited to measure stress stability in X-ray reflective thin film coatings. The coatings must be stable within 0.1 N/m or else they will cause the resolution of the telescope to fall out of specification. This work analytically models the silicon device and details causes of non-repeatability. Three mounting designs are discussed. This thesis demonstrates that a ± 0.01 N/m repeatability is possible for the technique on uncoated membranes. Without remounting the device between tests, an integrated stress standard deviation of the mean of ± 0.003 N/m with a 95% confidence interval. With remounting, preliminary testing has an integrated stress standard deviation of the mean of ± 0.034 N/m with a 95% confidence interval. According to these preliminary measurements, the device described in this work is superior to the existing substrate curvature measurement tools that have been developed both for industry and for research, which have published repeatability of ± 0.32 N/m and ± 1 N/m respectively.

### 8.0.1 Future Work

First, the non-repeatability caused by the laser position changing needs to be corrected by fixturing the kinematic holder in the vacuum chamber. Using a chamber with a flat bottom, instead of mounting inside a flange, would facilitate this. Repeatability testing for remounting can then be retested. Afterwards, coated membranes can be tested and the integrated stress measurements can be compared to curvature measurements of coated wafers using the Space Nanotechnology Laboratory's thin optics mount. Comparison with the curvature measurements should validate that the device can measure integrated stress in thin films to unprecedented levels of repeatability.

The glass holder would need to be redesigned for large-scale use of the device. Electrodes and traces could be patterned onto the glass to improve electrical connections and to better control the electrode spacing. The device could be affixed to the borosilicate glass by anodic bonding. Improved temperature control, such as by using a water-cooled chiller to control a coil inside the chamber, could be used to decrease non-repeatability due to temperature fluctuation. Additionally, stochastic input instead of swept sine input could potentially be used to reduce the time a frequency test takes to run.

# Bibliography

[1] O'Dell, S. L., Brissenden, R. J., Davis, W. N., Elsner, R. F., Elvis, M. S., Freeman, M. D., Gaetz, T., Gorenstein, P., Gubarev, M. V., Jerius, D., Juda, M., Kolodziejczak, J. J., Murray, S. S., Petre, R., Podgorski, W., Ramsey, B. D., Reid, P. B., Saha, T., Schwartz, D. A., Trolier-McKinstry, S., Weisskopf, M. C., Wilke, R. H. T., Wolk, S., and Zhang, W. W., 2010, "High-Resolution x-Ray Telescopes," A.M. Khounsary, S.L. O'Dell, and S.R. Restaino, eds., San Diego, California, United States, p. 78030H.

[2] Schwartz, D., and Gursky, H., 1974, "The Cosmic X-Ray Background," *X-Ray Astronomy*, R. Giacconi, and H. Gursky, eds., Springer Netherlands, Dordrecht, pp. 359–388.

[3] Wolter, H., 1952, "Spiegelsysteme streifenden Einfalls als abbildende Optiken für Röntgenstrahlen," Annalen der Physik, **445**(1–2), pp. 94–114.

[4] Wolter, H., 1952, "Verallgemeinerte Schwarzschildsche Spiegelsysteme streifender Reflexion als Optiken für Röntgenstrahlen," Annalen der Physik, **445**(4–5), pp. 286–295.

[5] Weisskopf, M. C., Tananbaum, H. D., Van Speybroeck, L. P., and O'Dell, S. L., 2000, "Chandra X-Ray Observatory (CXO):Overview," pp. 2–16.

[6] Zhang, W. W., Biskach, M. P., Blake, P. N., Chan, K. W., Evans, T. C., Hong, M. L., Jones, W. D., Kolos, L. D., Mazzarella, J. M., McClelland, R. S., O'Dell, S. L., Saha, T. T., and Sharpe, M. V., 2011, "Lightweight and High Angular Resolution X-Ray Optics for Astronomical Missions," *Optics for EUV, X-Ray, and Gamma-Ray Astronomy V*, SPIE, pp. 190–201.

[7] Zhang, W. W., Biskach, M. P., Blake, P. N., Bly, V. T., Carter, J. M., Chan, K. W., Gaskin, J. A., Hong, M., Hohl, B. R., Jones, W. D., Kolodziejczak, J. J., Kolos, L. D., Mazzarella, J. R., McClelland, R. S., McKeon, K. P., Miller, T. M., O'Dell, S. L., Riveros, R. E., Saha, T. T., Schofield, M. J., Sharpe, M. V., and Smith, H. C., 2013, "High Resolution and High Throughput X-Ray Optics for Future Astronomical Missions," *Optics for EUV, X-Ray, and Gamma-Ray Astronomy VI*, SPIE, pp. 231–243.

[8] Zhang, W. W., 2019, "High-Resolution, Lightweight, and Low-Cost x-Ray Optics for the Lynx Observatory," JATIS, **5**(2), p. 021012.

[9] "Chandra :: Resources :: Telescope System:: Mirror Fabrication" [Online]. Available: https://chandra.harvard.edu/resources/illustrations/mirrorFab.html. [Accessed: 21-May-2023].

[10] Madsen, K. K., Harrison, F. A., An, H., Boggs, S. E., Christensen, F. E., Cook, R., Craig, W. W., Forster, K., Fuerst, F., Grefenstette, B., Hailey, C. J., Kitaguchi, T., Markwardt, C., Mao, P., Miyasaka, H., Rana, V. R., Stern, D. K., Zhang, W. W., Zoglauer, A., Walton, D., and Westergaard, N. J., 2014, "The Nuclear Spectroscopic Telescope Array (NuSTAR) High-Energy X-Ray Mission," *Space Telescopes and Instrumentation 2014: Ultraviolet to Gamma Ray*, SPIE, pp. 489–499.

[11] Abermann, R., 1990, "Measurements of the Intrinsic Stress in Thin Metal Films," Vacuum, **41**(4), pp. 1279–1282.

[12] Seel, S. C., 2002, "Stress and Structure Evolution during Volmer-Weber Growth of Thin Films," Thesis, Massachusetts Institute of Technology.

[13] Gall, K., West, N., Spark, K., Dunn, M. L., and Finch, D. S., 2004, "Creep of Thin Film Au on Bimaterial Au/Si Microcantilevers," Acta Materialia, **52**(8), pp. 2133–2146.

[14] Windischmann, H., 1992, "Intrinsic Stress in Sputter-Deposited Thin Films," Critical Reviews in Solid State and Materials Sciences, **17**(6), pp. 547–596.

[15] Grachev, S., Hérault, Q., Wang, J., Balestrieri, M., Montigaud, H., Lazzari, R., and Gozhyk, I., 2022, "A New Method for High Resolution Curvature Measurement Applied to Stress Monitoring in Thin Films," Nanotechnology, **33**(18), p. 185701.

[16] Serlemitsos, P. J., Ogasaka, Y., Soong, Y., and Chan, K.-W., 1997, "Multilayer Option for Conical Foil X-Ray Mirrors," *Grazing Incidence and Multilayer X-Ray Optical Systems*, SPIE, pp. 244–252.

[17] Zhang, W. W., Bolognese, J., Byron, G., Chan, K. W., Content, D. A., Hadjimichael, T. J., He, C., Hill, M. D., Hong, M., Lehan, J. P., Lozipone, L., Mazzarella, J. M., McClelland, R., Nguyen, D. T., Olsen, L., Petre, R., Robinson, D., Rohrbach, S. O., Russell, R., Saha, T. T., Sharpe, M., Gubarev, M. V., Jones, W. D., O'Dell, S. L., Davis, W., Caldwell, D. R., Freeman, M., Podgorski, W., and Reid, P. B., 2008, "Constellation-X Mirror Technology Development," *Space Telescopes and Instrumentation 2008: Ultraviolet to Gamma Ray*, SPIE, pp. 43–52.

[18] Chan, K.-W., Sharpe, M., Zhang, W., Kolos, L., Hong, M., McClelland, R., Hohl, B., Saha, T., and Mazzarella, J., 2013, "Coating Thin Mirror Segments for Lightweight X-Ray Optics," *Optics for EUV, X-Ray, and Gamma-Ray Astronomy VI*, SPIE, pp. 339–350.

[19] Chalifoux, B. D., Yao, Y., Heilmann, R. K., and Schattenburg, M. L., 2019, “Simulations of Film Stress Effects on Mirror Segments for the Lynx X-Ray Observatory Concept,” JATIS, 5(2), p. 021004.

[20] Windt, D. L., 2007, “Reduction of Stress and Roughness by Reactive Sputtering in W/B4C x-Ray Multilayer Films,” *Optics for EUV, X-Ray, and Gamma-Ray Astronomy III*, SPIE, pp. 240–249.

[21] Broadway, D. M., Weimer, J., Gurgew, D., Lis, T., Ramsey, B. D., O’Dell, S. L., Gubarev, M., Ames, A., and Bruni, R., 2015, “Achieving Zero Stress in Iridium, Chromium, and Nickel Thin Films,” *EUV and X-Ray Optics: Synergy between Laboratory and Space IV*, SPIE, pp. 129–143.

[22] Broadway, D. M., Ramsey, B. D., O’Dell, S. L., and Gurgew, D., 2017, “In-Situ Stress Measurement of Single and Multilayer Thin-Films Used in x-Ray Astronomy Optics Applications,” *Optics for EUV, X-Ray, and Gamma-Ray Astronomy VIII*, SPIE, pp. 287–293.

[23] Mori, H., Okajima, T., Zhang, W. W., Chan, K.-W., Koenecke, R., Mazzarella, J. R., Numata, A., Olsen, L. G., Riveros, R. E., and Yukita, M., 2018, “Reflective Coatings for the Future X-Ray Mirror Substrates,” *Space Telescopes and Instrumentation 2018: Ultraviolet to Gamma Ray*, SPIE, pp. 1012–1019.

[24] Bishop, N. L., Kradinov, V., Reid, P. B., Jackson, T. N., DeRoo, C. T., and Trolier-McKinstry, S., 2022, “Stress-Balancing in Piezoelectric Adjustable x-Ray Optics,” JATIS, **8**(2), p. 029004.

[25] Chalifoux, B. D., 2019, “Figure Correction of Thin Plate and Shell Substrates Using Stress Generated by Ion Implantation,” Thesis, Massachusetts Institute of Technology.

[26] Zuo, H. E., 2021, “Ultrafast Laser Micromachining for Correction of Thin Optics for Next Generation X-Ray Space Telescopes,” Thesis, Massachusetts Institute of Technology.

[27] DeRoo, C. T., Allured, R., Cotroneo, V., Hertz, E. N., Marquez, V., Reid, P. B., Sr, E. D. S., Vikhlinin, A. A., Trolier-McKinstry, S., Walker, J., Jackson, T. N., Liu, T., and Tendulkar, M., 2018, “Deterministic Figure Correction of Piezoelectrically Adjustable Slumped Glass Optics,” JATIS, **4**(1), p. 019004.

[28] Yao, Y., Chalifoux, B. D., Heilmann, R. K., and Schattenburg, M. L., 2019, “Thermal Oxide Patterning Method for Compensating Coating Stress in Silicon Substrates,” Opt. Express, OE, **27**(2), pp. 1010–1024.

[29] Yao, Y., Chalifoux, B. D., Heilmann, R. K., Chan, K.-W., Mori, H., Okajima, T., Zhang, W. W., and Schattenburg, M. L., 2019, “Progress of Coating Stress Compensation of Silicon Mirrors for Lynx X-Ray Telescope Mission Concept Using Thermal Oxide Patterning Method,” JATIS, **5**(2), p. 021011.

[30] Solly, P. M., Zhang, W. W., Windt, D., and Yao, Y., 2022, "Coating of Thin, Lightweight x-Ray Mirrors without Distortion," *Space Telescopes and Instrumentation 2022: Ultraviolet to Gamma Ray*, SPIE, pp. 1197–1208.

[31] Aaltonen, T., Ritala, M., Sammelselg, V., and Leskelä, M., 2004, "Atomic Layer Deposition of Iridium Thin Films," J. Electrochem. Soc., **151**(8), p. G489.

[32] Aaltonen, T., Ritala, M., Sajavaara, T., Keinonen, J., and Leskelä, M., 2003, "Atomic Layer Deposition of Platinum Thin Films," Chem. Mater., **15**(9), pp. 1924–1928.

[33] Gaskin, J., "Technology Needs for LYNX: Mirrors, Coatings and Metrology."

[34] Akilian, M., Forest, C. R., Slocum, A. H., Trumper, D. L., and Schattenburg, M. L., 2007, "Thin Optic Constraint," Precision Engineering, **31**(2), pp. 130–138.

[35] Chalifoux, B., Sung, E., Heilmann, R. K., and Schattenburg, M. L., 2013, "High-Precision Figure Correction of x-Ray Telescope Optics Using Ion Implantation," *Optics for EUV, X-Ray, and Gamma-Ray Astronomy VI*, SPIE, pp. 292–304.

[36] Timoshenko, S., and Goodier, J. N., 1951, *Theory of Elasticity*, McGraw-Hill, New York.

[37] Stoney, G. G., and Parsons, C. A., 1997, "The Tension of Metallic Films Deposited by Electrolysis," Proceedings of the Royal Society of London. Series A, Containing Papers of a Mathematical and Physical Character, **82**(553), pp. 172–175.

[38] Janssen, G. C. A. M., Abdalla, M. M., van Keulen, F., Pujada, B. R., and van Venrooy, B., 2009, "Celebrating the 100th Anniversary of the Stoney Equation for Film Stress: Developments from Polycrystalline Steel Strips to Single Crystal Silicon Wafers," Thin Solid Films, **517**(6), pp. 1858–1867.

[39] Nix, W. D., 1989, "Mechanical Properties of Thin Films," Metall Mater Trans A, **20**(11), pp. 2217–2245.

[40] Chaudhari, P., 1969, "Mechanisms of Stress Relief in Polycrystalline Films," IBM Journal of Research and Development, 13(2), pp. 197–204.

[41] Chaudhari, P., 2003, "Hillock Growth in Thin Films," Journal of Applied Physics, **45**(10), pp. 4339–4346.

[42] Vinci, R. P., Zielinski, E. M., and Bravman, J. C., 1995, "Thermal Strain and Stress in Copper Thin Films," Thin Solid Films, **262**(1), pp. 142–153.

[43] Weiss, D., Gao, H., and Arzt, E., 2001, "Constrained Diffusional Creep in UHV-Produced Copper Thin Films," Acta Materialia, **49**(13), pp. 2395–2403.

[44] Zhou, S., Ji, Z., and Shao, T., 2015, "Residual Stress Evolution during Long-Term and Cyclic Aging and Annealing of Gold Films Deposited by Electron Beam Evaporation," Vacuum, **120**, pp. 132–138.

[45] Guan, D., Bruccoleri, A. R., Heilmann, R. K., and Schattenburg, M. L., 2013, "Stress Control of Plasma Enhanced Chemical Vapor Deposited Silicon Oxide Film from Tetraethoxysilane," J. Micromech. Microeng., **24**(2), p. 027001.

[46] Liu, D., and Flewitt, P. E. J., 2014, "Raman Measurements of Stress in Films and Coatings."

[47] Noyan, I. C., 1987, *Residual Stress: Measurement by Diffraction and Interpretation*, Springer-Verlag, New York.

[48] Berry, B. S., and Pritchet, W. C., 1990, "Internal Stress and Internal Friction in Thin-layer Microelectronic Materials," Journal of Applied Physics, **67**(8), pp. 3661–3668.

[49] Welzel, U., Ligot, J., Lamparter, P., Vermeulen, A. C., and Mittemeijer, E. J., 2005, "Stress Analysis of Polycrystalline Thin Films and Surface Regions by X-Ray Diffraction," J Appl Cryst, **38**(1), pp. 1–29.

[50] Schell-Sorokin, A. J., and Tromp, R. M., 1990, "Mechanical Stresses in (Sub)Monolayer Epitaxial Films," Phys. Rev. Lett., **64**(9), pp. 1039–1042.

[51] Chason, E., and Floro, J. A., 1996, "Measurements Of Stress Evolution During Thin Film Deposition," MRS Online Proceedings Library (OPL), **428**, p. 499.

[52] "FLX Flexus Thin Film Stress Measurement Systems TOHO Technology | Quantum Design" [Online]. Available: https://qd-europe.com/de/en/product/flx-flexus-thin-film-stress-measurement-systems/. [Accessed: 26-Apr-2023].

[53] "Product Specifications: KSA MOS UltraScan," k-Space Associates, Inc. [Online]. Available: https://k-space.com/document/product-specifications-ksa-mos-ultrascan/. [Accessed: 26-Apr-2023].

[54] "KSA MOS," k-Space Associates, Inc. [Online]. Available: https://k-space.com/product/mos/. [Accessed: 26-Apr-2023].

[55] Floro, J. A., Chason, E., Lee, S. R., Twesten, R. D., Hwang, R. Q., and Freund, L. B., 1997, "Real-Time Stress Evolution during Si1-XGex Heteroepitaxy: Dislocations, Islanding, and Segregation," J. Electron. Mater., **26**(9), pp. 969–979.

[56] Klokholm, E., 2003, "An Apparatus for Measuring Stress in Thin Films," Review of Scientific Instruments, **40**(8), pp. 1054–1058.

[57] "Thin Optic Surface Analysis for High Resolution X-Ray Telescopes" [Online]. Available: https://dspace.mit.edu/handle/1721.1/34556. [Accessed: 09-Feb-2020].

[58] Acosta, R. E., Maldonado, J. R., Towart, L. K., and Warlaumont, J. M., 1984, "B-Si Masks for Storage Ring X-Ray Lithography," *X-Ray Lithography and Applications of Soft X-Rays to Technology*, SPIE, pp. 114–118.

[59] Karnezos, M., 1986, "Effects of Stress on the Stability of X-ray Masks," Journal of Vacuum Science & Technology B: Microelectronics Processing and Phenomena, **4**(1), pp. 226–229.

[60] Maden, M. A., Jagota, A., Mazur, S., and Farris, R. J., 1994, "Vibrational Technique for Stress Measurement in Films: I, Ideal Membrane Behavior," Journal of the American Ceramic Society, **77**(3), pp. 625–635.

[61] Su, C. M., and Wuttig, M., 1993, "In-Situ Mechanical Relaxation of Cu Films Growing on a Si Substrate," Applied Physics Letters, **63**(25), pp. 3437–3439.

[62] Berry, B. S., Pritchet, W. C., and Uzoh, C. E., 1989, "Dynamical Method for the Thermomechanical Study of Thin Membranes," Journal of Vacuum Science & Technology B: Microelectronics Processing and Phenomena, **7**(6), pp. 1565–1569.

[63] Su, C. M., Wen, Y., and Wuttig, M., 1996, "Internal Friction in Thin Films and Membrane," J. Phys. IV France, **06**(C8), pp. C8-768.

[64] Rayleigh, J. W. S., 1877, *The Theory of Sound*, London, Macmillan and co.

[65] Ku, Y. C., Smith, H. I., and Plotnik, I., 1990, "Low Stress Tungsten Absorber for X-Ray Masks," Microelectronic Engineering, **11**(1), pp. 303–308.

[66] Timoshenko, S. P., and Winowsky-Krieger, S., 1959, *Theory of Plates and Shells*, McGraw-Hill, New York.

[67] Zhang, Y., 2016, "Large Deflection of Clamped Circular Plate and Accuracy of Its Approximate Analytical Solutions," Sci. China Phys. Mech. Astron., **59**(2), p. 624602.

[68] Wah, T., 1961, "Vibration of Circular Plates," The Journal of the Acoustical Society of America, **34**(3), pp. 275–281.

[69] Su, C. M., and Wuttig, M., 1994, "Internal Friction in Thin Films and Membranes," Journal of Alloys and Compounds, **211–212**, pp. 428–433.

[70] Fartash, A., Schuller, I. K., and Grimsditch, M., 1992, "Thin-film Modeling for Mechanical Measurements: Should Membranes Be Used or Plates?," Journal of Applied Physics, **71**(9), pp. 4244–4248.

[71] Batra, R. C., Porfiri, M., and Spinello, D., 2007, "Review of Modeling Electrostatically Actuated Microelectromechanical Systems," Smart Mater. Struct., **16**(6), p. R23.

[72] Wygant, I. O., Kupnik, M., and Khuri-Yakub, B. T., 2008, "Analytically Calculating Membrane Displacement and the Equivalent Circuit Model of a Circular CMUT Cell," *2008 IEEE Ultrasonics Symposium*, pp. 2111–2114.

[73] Oh, K. W., and Ahn, C. H., 2008, "Magnetic Actuation," *Comprehensive Microsystems*, Y.B. Gianchandani, O. Tabata, and H.P. Zappe, eds., Elsevier, Amsterdam;

[74] Toshiyoshi, H., 2008, "Electrostatic Actuation," *Comprehensive Microsystems*, Y.B. Gianchandani, O. Tabata, and H.P. Zappe, eds., Elsevier, Amsterdam;

[75] Fargas-Marques, A., Casals-Terre, J., and Shkel, A. M., 2007, "Resonant Pull-In Condition in Parallel-Plate Electrostatic Actuators," Journal of Microelectromechanical Systems, **16**(5), pp. 1044–1053.

[76] Barnes, A. C., Roberts, R. C., Tien, N. C., Zorman, C. A., and Feng, P. X.-L., 2011, "Silicon Carbide (SiC) Membrane Nanomechanical Resonators with Multiple Vibrational Modes," *2011 16th International Solid-State Sensors, Actuators and Microsystems Conference*, pp. 2614–2617.

[77] Berry, B. S., and Pritchet, W. C., 1991, "Stress and Thermal Expansion of Boron-doped Silicon Membranes on Silicon Substrates," Journal of Vacuum Science & Technology A, **9**(4), pp. 2231–2234.

[78] Hsueh, C.-H., 2002, "Modeling of Elastic Deformation of Multilayers Due to Residual Stresses and External Bending," Journal of Applied Physics, **91**(12), pp. 9652–9656.

[79] "Vibration Sensors & Probes | Fiber Optic MTI 2100 Fotonic Sensor," MTI Instruments [Online]. Available: https://mtiinstruments.com/products/non-contact-measurement/fiber-optic-sensors/fiber-optic-mti-2100-fotonic-sensor/. [Accessed: 17-May-2023].

[80] Blanding, D. L., 1999, *Exact Constraint: Machine Design Using Kinematic Principles*, ASME Press, New York.

[81] Soemers, H., 2010, *Design Principles for Precision Mechanisms*, Herman Soemers, Netherlands.

[82] "Vibrometry Products - VibroGo® Portable Laser Vibration Sensor from Polytec - Polytec" [Online]. Available: https://www.polytec.com/us/vibrometry/products/single-point-vibrometers/vibrogo. [Accessed: 18-May-2023].

[83] Zhao, Y., Trumper, D. L., Heilmann, R. K., and Schattenburg, M. L., 2010, "Optimization and Temperature Mapping of an Ultra-High Thermal Stability Environmental Enclosure," Precision Engineering, **34**(1), pp. 164–170.

[84] Sadeghian, H., Yang, C.-K., Gavan, K. B., Goosen, J. F. L., Drift, E. W. J. M. van der, Zant, H. S. J. van der, Bossche, A., French, P. J., and Keulen, F. van, 2010, "Some Considerations of Effects-Induced Errors in Resonant Cantilevers with the Laser Deflection Method," J. Micromech. Microeng., **20**(10), p. 105027.